ORIGINAL ARTICLE

Analysis and experimental validation of a pumped two-phase loop for multi-component electronics cooling

Myron Middelhuis[1] · Miguel Muñoz Rojo[1,2] · Wessel W. Wits[3]

Abstract

Miniaturization and enhanced performance of microchips has resulted in powerful electronic devices with high heat flux components. For these advanced electronics, the current heat transfer method of single-phase forced convection is reaching its thermal limit and more effective cooling solutions are needed. A pumped two-phase loop, in which a pump circulates a working fluid that evaporates to absorb heat, can offer a solution. In this paper the cooling performance of a pumped two-phase loop is discussed and validated. A numerical tool has been developed to aid in designing a fit-for-purpose pumped two-phase loop and to predict its behaviour to changing system parameters and heat inputs. Results from the numerical model are compared with temperature, pressure and flow velocity measurements obtained from a prototype setup. The effects of applying varying heat loads on both a single evaporator and on multiple evaporators simultaneously either in series or in parallel have been investigated. Heat transfer coefficients between 7 and 10 kW/m²K were obtained during the experiments. Model predictions correspond well to the measured performances and findings on the two-phase boiling behaviour are presented. The model is particularly useful for the rapid assessment of the layout of a pumped two-phase loop for high heat flux electronics cooling.

Nomenclature

μ_l	Liquid dynamic viscosity [Pa·s]
μ_v	Vapour dynamic viscosity [Pa·s]
ρ_l	Liquid density [kg/m³]
ρ_v	Vapour density [kg/m³]
A	Cross sectional area [m²]
A_s	Surface area [m²]
c_{tm}	Specific heat of thermal mass [J/kgK]
d	Channel diameter [m]
E_{cv}	Energy present in control volume [J]
F_{fric}	Frictional force [N]
$F_{gravity}$	Gravitational force [N]
g	Gravitational acceleration [m/s²]
h	Heat transfer coefficient [W/m²K]
H	Specific enthalpy [J/kg]
H_{lv}	Latent heat of vaporization [J/kg]
k	Thermal conductivity [W/mK]
K_L	Minor loss coefficient [-]
L	Channel length [m]
m_{cv}	Mass present in control volume [kg]
m_{tm}	Thermal mass (evaporator) [kg]
$\dot{m}$	Mass flow rate [kg/s]
P	Pressure [Pa]
P_{acc}	Accumulator pressure [Pa]
q	Heat input [W]
q''	Heat flux [W/m²]
$\dot{Q}$	Rate of heat transfer [W]
$\dot{Q}_{hc}$	Heat generated by heating cartridge [W]
t	Time [s]
T_b	Evaporator block temperature [K]
T_c	Cooling water temperature [K]
T_f	Working fluid temperature [K]
T_t	Evaporator tube temperature [K]
T_{tm}	Temperature of thermal mass [K]
u	Fluid flow velocity [m/s]
U	Overall heat transfer coefficient [W/m²K]
V_{acc}	Accumulator volume [m³]
W	Mechanical work done on working fluid [W]
x	Distance between thermocouples [m]
z	Height with respect to a reference level [m]

✉ Wessel W. Wits
W.W.Wits@utwente.nl

1   Thermal and Fluid Engineering, University of Twente, 7500 AE Enschede, Netherlands

2   2D Foundry, Instituto de Ciencia de Materiales de Madrid (ICMM), CSIC, Madrid 28049, Spain

3   Mathematics of Multiscale Modeling and Simulation, University of Twente, 7500 AE Enschede, Netherlands

☸ Springer

1 Introduction

1.1 Background

In recent decades, electronic devices have become increasingly smaller and more powerful. This has been facilitated by advances in the production of microprocessors, amongst others by approximately doubling the number of transistors on a chip, as predicted by Moore's law [1]. However, miniaturisation of chips and increasing processing speed decreases the heat transfer surface area and increases power consumption, causing higher heat flux densities. This poses great challenges to thermal management technologies in order to maintain operation within acceptable safety ranges [2]. For some general electronic devices like personal computer CPUs and server racks, traditional air cooling can be sufficiently effective in solving the thermal challenges by optimizing the heat sink design [3]. However, for advanced high-performance electronics devices, the current heat transfer method of forced air convection is reaching its limit and more effective cooling solutions are needed [2, 4].

Next to conventional thermal management approaches using convection based on air or coolant circulation, for cooling high power density electronics the application of a phase-transitional method is a promising technology [5]. Such two-phase cooling systems rely on absorption and release of heat by evaporation and condensation, respectively, of a working fluid. This technique exploits the latent heat of the working fluid, which is orders of magnitude higher than the sensible heat used in conventional convection-based systems. As a consequence, the working fluid's mass flow rate can be significantly decreased, opening opportunities for smaller and more efficient cooling systems [6]. Furthermore, as obtainable heat transfer coefficients in evaporative systems are much larger, component temperatures can be kept at a lower level as well.

Lately, industry has readily adopted passive two-phase systems in the form of heat pipes [7]. These are hermetically sealed enclosures, commonly metal tubes, with a wick structure at the inner walls capable of transporting the working fluid by capillary forces. Although very efficient, heat pipes are limited in heat transport capability in terms of size, shape and length due to frictional and body forces [8]. As a solution, variants of conventional heat pipes, such as loop heat pipes, capillary pumped loops and pulsating heat pipes, have found market entry for specific niches [7]. In all cases however, the wick structure and associated capillary pumping capacity poses a serious restriction on terrestrial applications for relatively large or vertically oriented systems and systems in motion [9]. Also, the start-up behaviour, temperature control and cooling of multiple components are precarious with passive two-phase systems [10]. To overcome these issues, a mechanically-driven two-phase system, in which a pump rather than a wick structure circulates the working fluid through the system, can offer a solution. Such a system can effectively cool microchips using cold plates [6] or by integrating the cooling channels directly into the PCB [8]. Compared to a single-phase system, the lower mass flow rate requires less pumping power, reducing the power consumption footprint as well. The pump however has a drawback that, next to careful dimensioning, internal pressure fluctuations due to evaporation of the working fluid must be compensated for. This paper addresses this both numerically and experimentally for a system in which multiple parallel evaporators are applied for the cooling of multiple components.

1.2 Literature review

Preliminary studies on two-phase heat transfer started in the 1980s in the USSR [11]. In the 1990s, work on two-phase pumped loops was continued for application on the Mir-2 space station [12]. Meanwhile, developments of aerospace-related mechanically pumped two-phase heat transfer systems took place at NASA [13, 14]. At the turn of the century, a mechanically pumped two-phase loop with ammonia as working fluid for the thermal control system for the International Space Station (ISS) was proposed by Bednov et al. [15]. Similarly, an application was proposed for the Alpha Magnetic Spectrometer (AMS-02) on the ISS by Delil et al. [16]. In this system, carbon dioxide (CO_2) was used as working fluid to keep the particle detector at a very stable temperature.

In 2008, the use of pumped two-phase loops in terrestrial applications was reported by Verlaat et al. [17]. They concluded that a pumped two-phase system with a controlling accumulator and CO_2 as working fluid would be a good candidate for the ATLAS detector at CERN. In 2010, Sharar et al. [6] reviewed the potential of a pumped two-phase loop for army vehicle applications. Similarly, Van Es and Van Gerner [18] discussed the benefits and drawbacks for its use in military platforms in 2013. Currently, the technology has also been adopted for cooling of high heat load electronics typically found in data-centre environments [19]. In 2019, Zhang et al. [20] reviewed the latest technological applications and reported a lack of knowledge on the effect of system elements such as the pump and reservoir, working fluid properties and temperature control methods. The numerical and experimental approach of this paper seeks to address this lack of knowledge.

Despite difficulties in predicting two-phase flow behaviour and challenges involved in flow boiling in small channels, two-phase loops have been used successfully in practice [19, 21]. So far, research has mainly focussed on

understanding the behaviour of flow boiling and understanding the behaviour of a pumped two-phase cooling system as a whole by numerical modelling and testing. Jie et al. [22] developed a pumped two-phase cooling system with CO_2 as working fluid and focussed on the robustness and reliability of the system with multiple evaporators. The effects of unbalanced heat loads and recovery from dry-out conditions were investigated. Lee and Park [23] worked on a hybrid two-phase loop, in which both a pump and capillary pressure were applied to transport the liquid. They created an experimental setup with methanol as working fluid and built a thermal-hydraulic network model, in which the mass, momentum and energy equations were simultaneously solved at eight locations (nodes) in the loop. Van Gerner and Braaksma [21] developed a model based on simplified one-dimensional Navier-Stokes equations, which were solved using the MacCormack predictor-corrector scheme. This model focussed on the transient behaviour of a pumped two-phase system and was validated by an experiment using CO_2 as working fluid. Mass flow and saturation temperatures at the condenser could be predicted accurately, yet a mismatch in the PID-controlled accumulator behaviour was present. Nevertheless, a very high temperature stability was achieved.

Recently, Meng et al. [24] investigated the transient behaviour of a pumped two-phase loop with an active, thermally controlled accumulator using propane as working fluid. Transient effects during start-up of the system and due to turning heat loads on and off were investigated. It was shown that during heat source load-on and load-off conditions, oscillations of temperature and pressure in the accumulator took place before the pumped loop returned to stable operating conditions. Similar research was performed by Li et al. [25], in which an experimental setup using acetone was built. They found that pressure oscillations and temperature overshoot phenomena occur at the evaporator outlet when the system shifts from single-phase to two-phase after start-up.

1.3 Scope and approach

The work presented in this paper extends the aforementioned fundamental research into flow boiling and two-phase cooling systems. A first attempt to the development of a design tool for a pumped two-phase loop is presented. To this extent, a fast and user-friendly numerical model has been built that determines the effects of the system design as a whole and its operating conditions on the system's performance. Furthermore, the effects of specific design parameters such as accumulator volume, flow rate and channel layout can be predicted. This provides a sound understanding of the system's response to changing conditions and allows for fast design iterations as well. The model is based on a control

volume approach, in which mean thermophysical properties are determined for each element of the pumped two-phase loop. The basic modelling elements include the pump, accumulator, evaporator, condenser and fluid transport channels. These basic elements can be connected to model conceptual system configurations. This makes the developed numerical tool useful for making preliminary design choices for a pumped two-phase cooling system. To test the performance of an actual system, a prototype pumped two-phase loop has been built. Finally, the numerical results of the developed model are compared to the experimental results.

2 Methodology

2.1 Operating principle

The challenge of describing a pumped two-phase loop is in the interaction between the system components and how the system reacts to changing operation conditions, such as the heat load. This is illustrated in Fig. 1. The figure depicts an evaporator and a condenser in a loop. A pump continuously propels the working fluid through the loop. Finally, to manage the effect of working fluid expansion, an accumulator is attached to the loop just before the pump. Figure 1(a) depicts the system operational mode with a constant flow rate of 0.2 l/min, but without any heat load. When the heat input is increased, as shown in Fig. 1(b), a part of the liquid flow starts to evaporate in the evaporator section. Since the vapour density is much lower than that of the liquid, the fluid expands significantly and the flow velocity increases, in this exemplary case for CO_2 to 0.6 l/min. The expansion process causes a liquid/vapour front to travel through the loop, at which location the vapour velocity and pressure are increased. The liquid/vapour front pushes the liquid ahead of the front into the accumulator, in this example at a rate of 0.4 l/min as the pump continues to operate at a constant flow rate of 0.2 l/min. When the liquid/vapour front reaches the condenser, the vapour returns to its liquid form, and the velocity at the end of the condenser returns to the initial flow value of the loop set by the pump, as shown in Fig. 1(c). The two-phase loop has now reached a new equilibrium state with more liquid being present in the accumulator. This increases the system pressure, as non-condensing gas present in the accumulator is being compressed. The opposite process takes place when the heat load is decreased. Although the main system pressure is dictated by the accumulator, local differences occur in the loop due to fluid expansion and pipe friction. In order to predict the effects of changing heat loads on the system, a transient model is required that describes the system states when altering between steady-state operating conditions (i.e. switching between heat loads).

Fig. 1 Illustration of pumped two-phase loop operating principle, edited from Bolder [26]: **a** and **c** illustrate the equilibrium states at zero and high power, respectively, while in **b** the system is still in transition witnessed by a moving vapour/liquid front and changing accumulator fill ratio
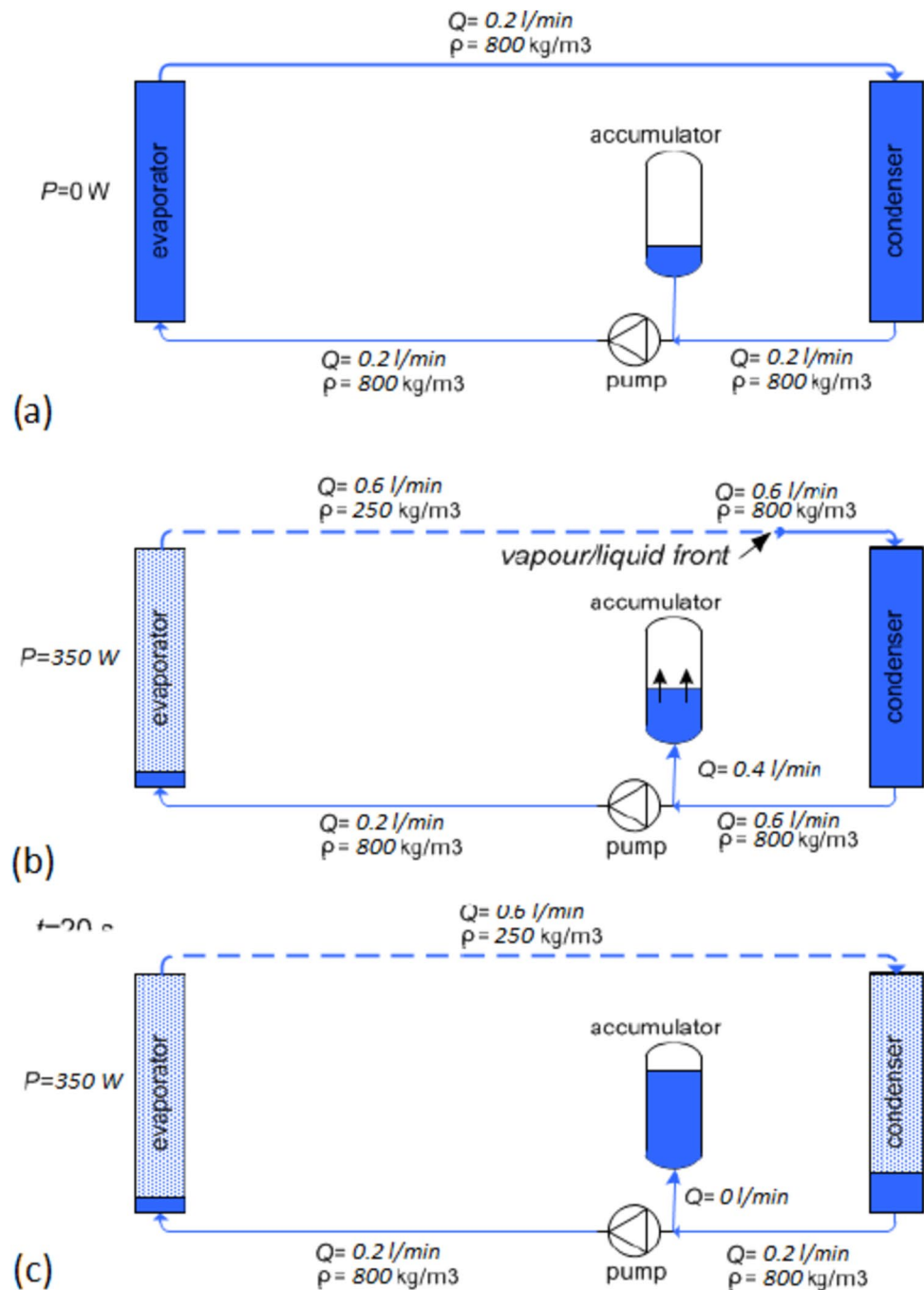
2.2 Working fluid selection

Due to its high heat capacity, water would be a safe and effective working fluid. However, as documented by Hoang et al. [5], it is challenging to implement two-phase cooling with water due to the high boiling point of water at atmospheric pressure. Most types of electronics cannot tolerate these high junction temperatures [5]. Therefore, an alternative working fluid was selected using a Figure Of Merit (FOM) approach, in which an assessment criterion is

defined based on a number of performance requirements. This assessment criterion provides a score over a range of temperatures for each investigated fluid [27]. For a pumped two-phase loop, the flow resistance and the heat transfer rate should be considered, as the pump needs to supply enough pressure head to overcome the total friction in the loop [24]. Van Gerner et al. [27] have proposed an expression for the FOM for a pumped two-phase loop, given by Eq. 1. In this equation μ is the dynamic viscosity, ρ the density and H_{lv} the latent heat of vaporization of the working fluid. The

subscripts l and v indicate the (saturated) liquid and (saturated) vapour states of the working fluid, respectively.

$$FOM = \frac{1}{\mu_l^{\frac{1}{4}} / \left(\rho_l H_{lv}^{\frac{7}{4}} \right) + \mu_v^{\frac{1}{4}} / \left(\rho_v H_{lv}^{\frac{7}{4}} \right)} \quad (1)$$

Several commonly used working fluids were compared by determining their FOM over a temperature range from 10 °C to 90 °C, which is typical for electronics cooling, see Fig. 2. Overall, ammonia would perform best, yet this fluid was in this case not chosen due to its toxicity. CO_2 was found to be a high-performance candidate on temperatures lower than its critical temperature of 31 °C. As a natural working fluid, CO_2 is non-explosive, non-flammable, non-toxic and relatively low cost. Furthermore, it has no ozone depletion potential (ODP = 0) and a negligible direct global warming potential (GWP = 1) when used as a working fluid [28]. These considerations made CO_2 the working fluid of choice for this study.

2.3 Evaporator channel dimensioning

The size of the evaporator channels is critical for flow boiling behaviour. It is therefore important to distinguish between macrochannels and microchannels, since the transport phenomena are significantly different [29]. Flow in macrochannels experiences a strong dependence on gravity, while flow in microchannels is hardly affected by gravity, and depends mostly on surface tension and capillary action. A number of definitions exists in literature for the distinction

between microchannels and macrochannels, but universal agreement is lacking. In general, a consensus for most definitions yields a hydraulic diameter of around 6 mm as the distinctive threshold between micro- and macrochannels for water and around Ø3 mm for CO_2 [30–32]. For cooling applications in high heat-flux, densely packed electronics, Mudawar [33] recommends the use of microchannel cooling. This study has a similar focus and hence a microchannel design was pursued for the evaporator channels.

3 Numerical model of the two-phase system

In order to investigate the transient behaviour of a pumped two-phase system and to test the effects of changing system parameters, a numerical model has been built in Simulink, a MATLAB-based graphical programming environment. The aim was to use a modular and graphical approach, in which each component of the loop is represented by its own sub-system element, as shown in Fig. 3. In this way, alternative configurations can easily be simulated by selecting the appropriate sub-system elements and without altering the underlying code. In this case, Fig. 3 shows an exemplary configuration with four evaporator lines in parallel with each two evaporator blocks in series. The evaporator sub-system elements describe heat absorption from for instance electronic components that require active cooling. Multiple layouts with evaporators in series and/or in parallel can be analysed following this modular approach. The condenser sub-system element describes heat transfer from the working fluid to, in this particular case, a reservoir of cooling water.
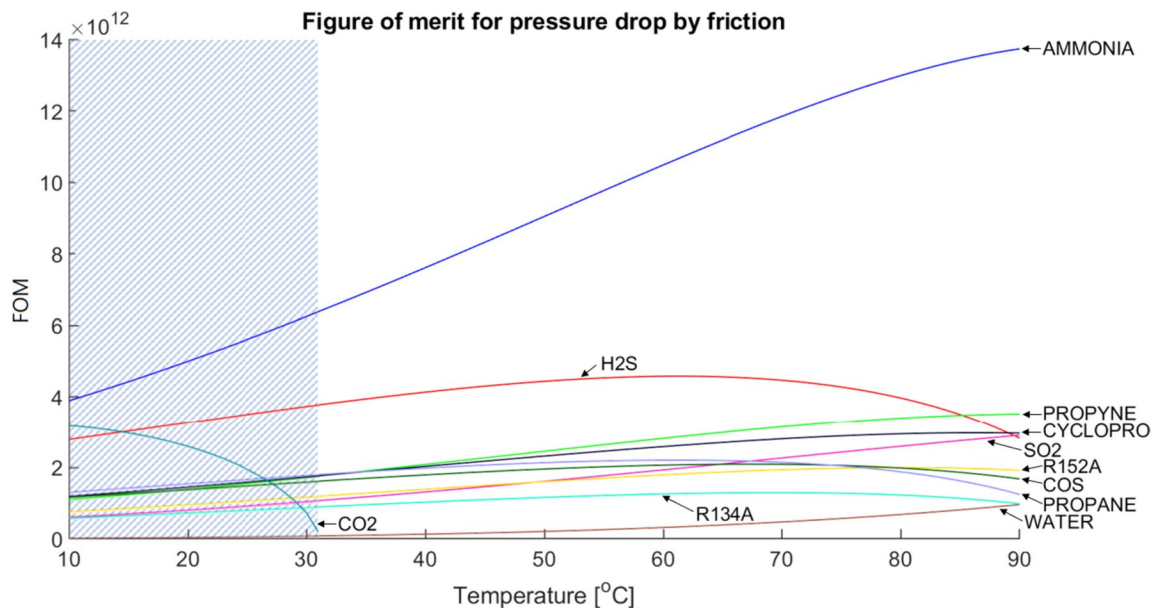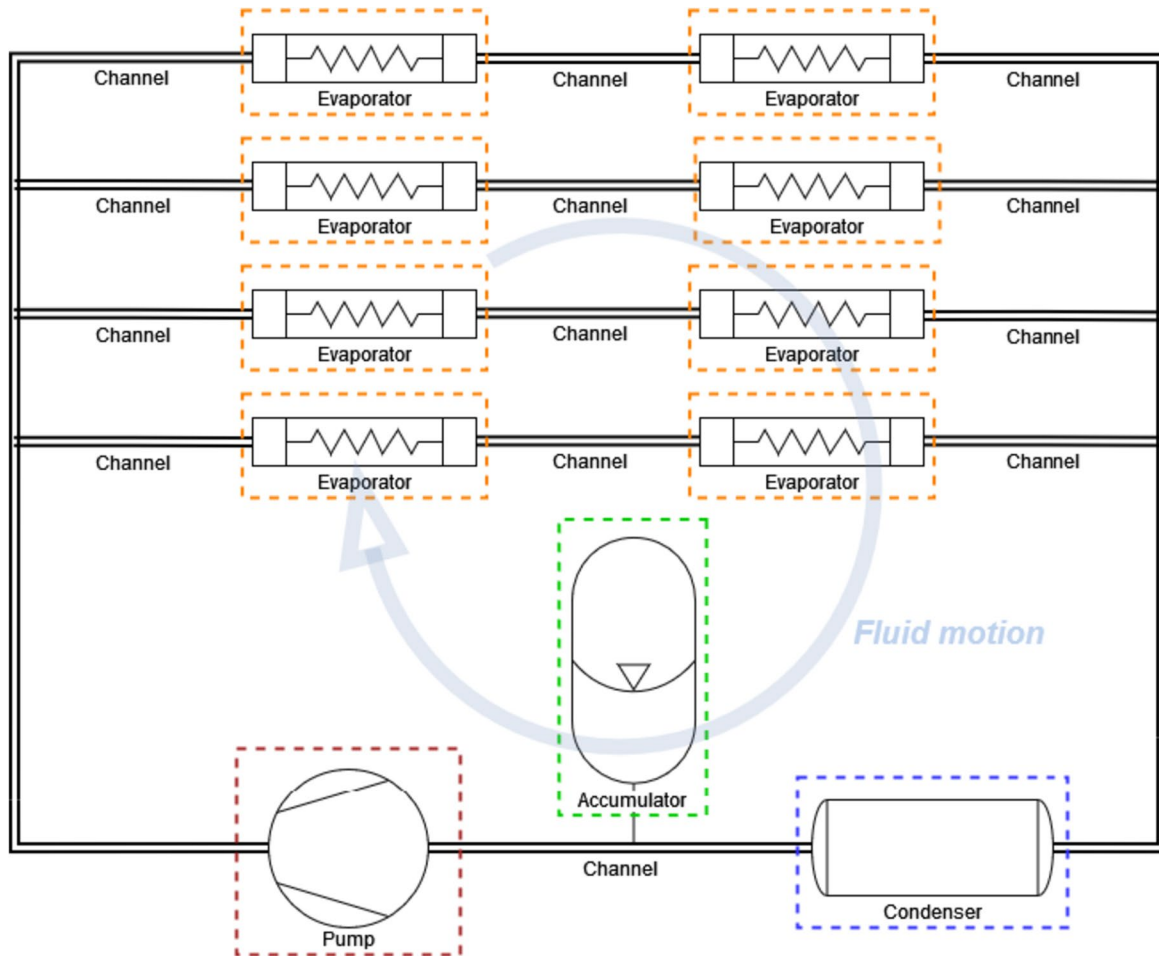

Fig. 2 Figure of merit for several commonly used working fluids following Eq. 1

Fig. 3 Schematic overview of the applied modular modelling approach and modelled sub-system elements

The accumulator sub-system element models the effect of fluid in- or outflow due to fluid expansion and relates this to the system pressure. The pump sub-system element determines the pressure required at the beginning of the loop in order to overcome frictional losses in the system for a set flow rate. Finally, transport channels model the working fluid circulation by interconnecting all sub-system elements into a loop.

3.1 Model theory

To describe all components of the pumped two-phase loop, a control volume method is used for deriving the governing equations. For a fixed control volume with well-defined boundaries, the control volume method significantly reduces the complexity of the mass, momentum and energy conservation equations. In this case, the boundaries are set by the geometric design of the components; e.g. volume, cross-sectional area and length. The conservation laws can be formulated in algebraic form rather than in integral form

[34, 35]. The resulting general algebraic equations for mass, momentum and energy conservation are given by Eqs. 2–4, respectively.

$$\frac{dm_{cv}}{dt} = \dot{m}_{in} - \dot{m}_{out} \tag{2}$$

$$\frac{d(mu)_{cv}}{dt} = \dot{m}_{in}u_{in} - \dot{m}_{out}u_{out} + P_{in}A_{in} - P_{out}A_{out} - F_{fric} - \cancelto{0}{F_{gravity}} \tag{3}$$

$$\frac{dE_{cv}}{dt} = \dot{m}_{in}\left(H + \cancelto{0}{\frac{u^2}{2}} + \cancelto{0}{gz}\right)_{in} - \dot{m}_{out}\left(H + \cancelto{0}{\frac{u^2}{2}} + \cancelto{0}{gz}\right)_{out} + \dot{Q}_{net,in} + \cancelto{0}{\dot{W}_{net,in}} \tag{4}$$

In these equations, $\dot{m}$ indicates the mass flow rate, u the fluid velocity, P the system pressure and A the cross-sectional area of the channels. F_{fric} is the force due to wall friction acting on the fluid and $F_{gravity}$ the force exerted on the fluid by gravity. In the energy equation, H is the fluid's enthalpy, g the gravitational acceleration and z height with

respect to a reference level. $Q_{net}^{.}$ indicates the net rate of heat transfer to the fluid and W_{net} is the net mechanical work done on the fluid.

Note that in the definition of Eqs. 2–4, it is assumed that flow at the in- and outlets is uniform and work due to viscous forces is neglected in the energy conservation equation. In mixture regions, both the liquid and vapour phases are assumed to be in the saturated state and move with the same velocity. The transport channels are considered adiabatic, hence there is no heat transfer with the environment. Since the prototype setup is largely oriented horizontally and total height differences are less than 0.5 m, gravitational effects (i.e. $F_{gravity}$ and gz) are ignored, as indicated in Eqs. 3 and 4. Furthermore, the contribution of kinetic energy (i.e. $u^2/2$) is neglected in Eq. 4, as this effect is negligible compared to the fluid's enthalpy. Finally, since work done by the pump is small compared to the heat input at the evaporator section, the mechanical work is ignored as well in Eq. 4. For instance, in the case where 100 W is applied to the evaporator, the increase in enthalpy by kinetic energy is 75× smaller than the increase in enthalpy by heat input, while the increase in enthalpy due to mechanical work by the pump is 2500× smaller.

3.2 Model implementation

For sub-system elements in which heat transfer takes place, as e.g. in the evaporator and condenser elements, all conservation laws need to be applied, while for the adiabatic transport channels the energy equation is not needed. In sub-system elements with short channels, like the evaporator, frictional losses are ignored. In order to connect all elements that make up a two-phase loop and to transfer properties between the elements, the state of the system at each element is defined by three parameters: enthalpy, pressure and velocity. Enthalpy and pressure are the state variables that determine the (local) fluid properties of the system. Based on a given enthalpy and pressure, other fluid properties are obtained using the NIST REFPROP database [36]. This also applies to the vapour quality, which is defined as the mass fraction of vapour in the liquid–vapour mixture. The velocity serves as an indirect measure for the mass flow rate in the system and is used to compute frictional losses between sub-system elements.

Figure 4 illustrates the control volumes that are used to derive the governing equations for the evaporator, condenser and transport channels. Based on the generic conservation Eqs. 2–4 and taking into account the aforementioned assumptions, the local conservation equations for mass, momentum and energy are derived, see Eqs. 5–7, respectively. In these equations, the mass flow rate is written as the product of density and velocity, while the friction forces at the channel walls result in a pressure loss

in the momentum equation. The density is constant for each time integration step and the outgoing variables (with subscript out in Eqs. 2–4) are the control volume variables of the previous time integration step. The energy equation is written in terms of enthalpy, since the fluid parameters are based on the local enthalpy and pressure. Furthermore, the advantage of using enthalpy is that subcooled liquid and superheated vapour can be determined in the model without additional computational steps.

$$AL\frac{d}{dt}(\rho) = Au_{in}\rho_{in} - Au\rho \tag{5}$$

$$AL\frac{d}{dt}(\rho u) = Au_{in}^2\rho_{in} - Au^2\rho + A\Delta P - A\Delta P_{fric} \tag{6}$$

$$AL\frac{d}{dt}(\rho H) = \dot{Q}_{in} + Au_{in}\rho_{in}H_{in} - Au\rho H \tag{7}$$

The rate of heat transfer to the working fluid $Q_{in}^{.}$ in the evaporator is determined by a heat balance between the working fluid and the thermal mass of the evaporator, see Eq. 8. Here, $A_{s,evap}$ is the surface area of the evaporator's microchannels, T_f is the temperature of the working fluid and T_{tm} the temperature of the thermal mass. The latter is computed by Eq. 9, in which $Q_{hc}^{.}$ is the heat input rate to the system, and m_{tm} and c_{tm} the mass and thermal capacity of the thermal mass, respectively.

$$\dot{Q}_{in} = hA_{s,evap}(T_{tm} - T_f) \tag{8}$$

$$\frac{d}{dt}(T_{tm}) = \frac{\dot{Q}_{hc} - \dot{Q}_{in}}{m_{tm}c_{tm}} \tag{9}$$

The heat transfer coefficient h in Eq. 8 is kept constant for each simulation run. In practice however, the heat transfer coefficient changes with heat flux, saturation temperature and mass flow rate. Empirical relations that predict the heat transfer coefficient depending on local two-phase flow conditions are known to have error margins up to 30% [37]. Hence, to quickly evaluate system layouts, as is the goal of the numerical model, using a constant heat transfer coefficient is sufficiently accurate. Moreover, validation of the model using experimental data is more convenient this way. As a consequence however, in the actual prototype setup the heat transfer coefficient will drop during cool down of the evaporator, as the heat flux decreases. Since in the numerical model the heat transfer coefficient is constant, a faster evaporator cool-down effect will be predicted. This effect can be found when comparing the output from the numerical model with the actual system response. For the purpose of this numerical model this effect is however negligible.
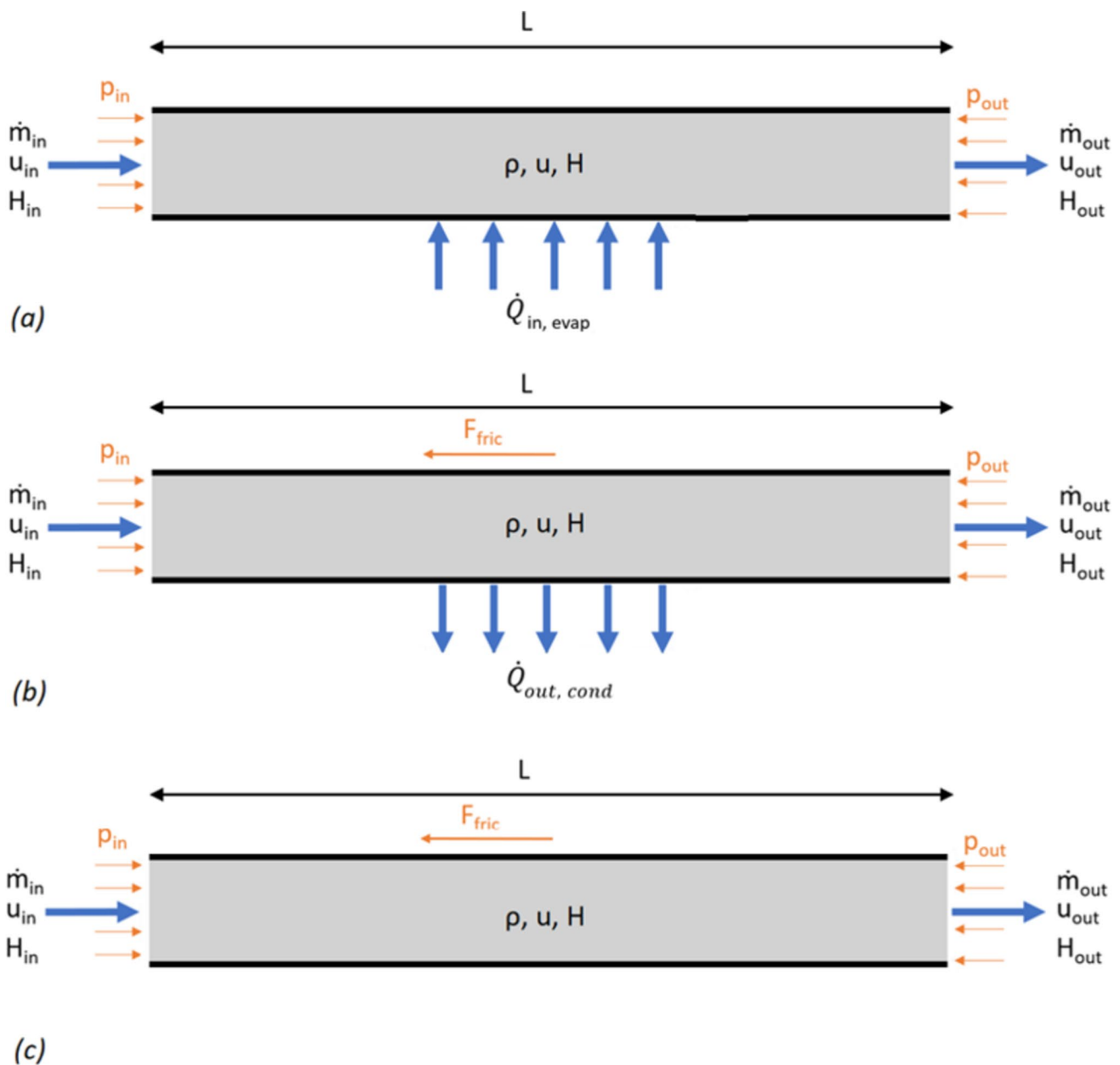
Fig. 4 Control volume model for the evaporator (**a**), condenser (**b**) and adiabatic transport channel (**c**)

In the condenser, the outgoing heat transfer rate $\dot{Q}_{out}$ is determined similarly following Eq. 10. In this equation U is the overall heat transfer coefficient between the working fluid and the cooling water and T_c the temperature of the coolant. In the prototype setup, the condenser consists of a copper spiral running through a vessel of cooling water, hence T_c is the cooling water temperature. $A_{s,cond}$ is the total surface area of the condenser spiral. To determine the overall heat transfer coefficient, the Dittus–Boelter correlation is used to calculate the heat transfer rate from the liquid CO_2 to the inner tube wall and the external heat transfer rate can be approximated as natural convection over a horizontal cylinder.

$$\dot{Q}_{out} = UA_{s,cond}(T_f - T_c) \tag{10}$$

Since the outputs of a control volume element are the fluid properties at the outlet, no information is obtained about what happens inside the control volume. This is problematic for the condenser, as the friction inside the element depends on the vapour quality and fluid velocity inside the element. As was illustrated in Fig. 1 (c), when heat is added

to the system, the vapour fraction inside the condenser element starts to increase as the vapour does not immediately condense when it reaches the condenser. This increasing vapour fraction causes the liquid that is present to be pushed forward, increasing the output velocity. When only one control volume element is used to model the condenser, these effects are ignored. Therefore, the condenser element in the numerical model is split in several sub-elements. Iteratively, it was determined that a total of 10 sub elements provides a good balance between computational time and accuracy.

In order to determine the pressure loss due to friction in the transport channels and the condenser, the two-phase pressure loss correlation by Müller-Steinhagen and Heck was applied [38]. Xu et al. [39] reviewed 29 correlations and compared them with 3480 experimental data points, and found this correlation the most accurate. The correlation by Müller-Steinhagen and Heck is essentially an empirical two-phase extrapolation between all-liquid flow and all-vapour flow. Therefore, this relation can be applied to each transport channel and condenser sub-element in the pumped-two phase loop model, whether the flow is two-phase or single-phase.

In accordance to the actual setup, the system pressure in the model is dictated by the accumulator. A passive membrane accumulator is used in which the pressure increases when working fluid enters the accumulator. At the gas side of the membrane an inert gas (typically nitrogen) is present, which is being compressed when liquid enters the accumulator. This is illustrated in Fig. 5. Before the system is pressurized, the accumulator is in State 0, in which the accumulator gas is at the prefill pressure P_0. P_0 should be lower than the desired system pressure. When the system is pressurized, some liquid CO_2 is present in the accumulator as illustrated by State 1 at the initial time $t=0$. During operational conditions, the accumulator will absorb more liquid

when expansion takes place in the system. This results in an increase of system pressure as the nitrogen gas is being compressed. This is depicted by accumulator State 2 in Fig. 5.

The amount of liquid CO_2 that flows into or out of the accumulator is determined by the velocity at the accumulator inlet u_{in} minus the flow velocity in the loop u_{out}, as dictated by the pump. As the liquid entering the accumulator is considered incompressible, the gas volume rate of change is given by Eq. 11, where V_{acc} represents the volume of gas present in the accumulator and A_{acc} the cross-sectional area of the accumulator inlet tube. Integrating this relation with respect to time yields the accumulator gas volume $V_{acc\,(t)}$ at time t. Using the ideal gas law for constant temperature conditions, the accumulator pressure at this time instance $P_{acc\,(t)}$ can be computed by Eq. 12.

$$\frac{dV_{acc}}{dt} = -\left(u_{in} - u_{out}\right)A_{acc} \tag{11}$$

$$P_{acc(t)} = \frac{P_{acc(t=0)}V_{acc(t=0)}}{V_{acc\,(t)}} \tag{12}$$

The pump itself is assumed to deliver a constant flow velocity, which can be set in the model. To do so, the pump needs to deliver enough pressure to overcome the frictional losses in the system. Since the frictional losses depend on the flow velocity and vapour-liquid mixture fraction of the complete loop [40], the model can only compute the total pressure loss at the pump inlet at the end of the loop. In practice, the system pressure at the pump inlet is set by the accumulator. Hence, the differential pressure generated by the pump should be sufficient to yield a pump inlet pressure equal to the accumulator pressure. To smoothly correct for changing pressure losses in the system (e.g. when the heat load at the evaporator changes), the difference between the

Fig. 5 Schematic overview of the accumulator operating principle. From left to right: State 0 as installed at prefill pressure P_0, State 1 at initial working pressure $P_{(t=0)}$, and State 2 at operating pressure $P_{(t)}$
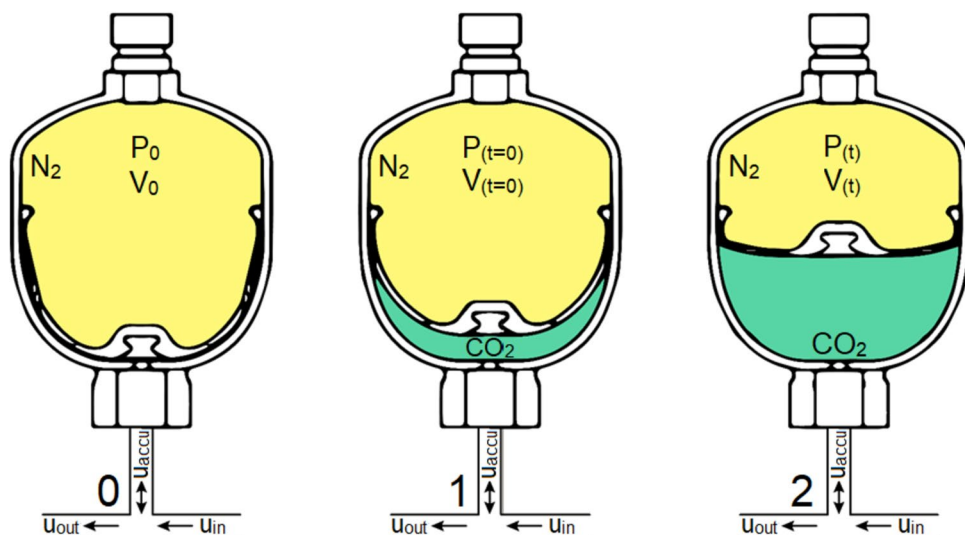
accumulator pressure and the pressure at the pump inlet is fed to a PI controller. This controller determines the required output pressure at the pump to obtain the correct system pressure at the pump inlet, which should be equal to the accumulator pressure.

Reducer sub-system elements are used when channels with different internal diameters are connected. This occurs for example at the connection between the evaporator channels with an internal diameter of 2 mm and the transport channels with an internal diameter of 4 mm. Pressure losses in reducing fittings can be determined using Eq. 13, in which K_L is the minor loss coefficient, as defined by Çengel and Cimbala [41]. The minor loss coefficient is a function of the ratio between the internal diameters of the connected pipes squared (d_1^2/d_2^2), where d_1 and d_2 are the inner diameters of the smaller and larger channel, respectively.

$$\Delta P_L = \frac{1}{2}\rho u^2 K_L \tag{13}$$

For the afore reducer elements, the minor loss coefficient is 0.3 when the channel diameter is reduced and 0.4 when the channel diameter is increased [41]. In order to evaluate the impact of the reducer's minor loss terms of the prototype setup, an exemplary case is assumed in which a total heat input of 100 W is applied on a single evaporator channel, while the pump circulates the working fluid at 300 ml/min. In this case, the simulation predicts a total system pressure drop of about 9 kPa, which must be delivered by the pump. At the evaporator section the working fluid enters at 1.5 m/s with a fluid density of 770 kg/m³, which, following Eq. 13,

results in a pressure loss of 260 Pa; i.e. 3% of the total loss. Similarly, at the evaporator exit the two-phase fluid has an average density of 625 kg/m³ and a velocity of 1.8 m/s, resulting in a pressure loss of 400 Pa; i.e. 4% of the total loss. As the reducer's pressure losses are relatively small, they may be ignored in the numerical model, which allows the reducer's output velocity to be solely dependent on the cross-sectional differences of the connected channels.

An overview of the Simulink model for the prototype setup is shown in Fig. 6. As aforementioned all components are coupled by the state variables H, P and u.

The algebraic forms of the conservation laws are all first-order Ordinary Differential Equations (ODEs) in time. Because some terms in the equations (e.g. flow velocity, fluid enthalpy) may lead to rapid variations in the solution space, the model can be classified as a stiff problem. The differential equations are numerically integrated in Simulink using MATLAB's ODE15s solver, which is accurate for stiff problems [42]. At each time step, local fluid properties for the sub-system elements are updated based on the fluid enthalpy and pressure at that element. A numerical analysis of a 10-min run of a single-evaporator loop corresponding to Fig. 6 can be performed in about 30 s on a regular desktop PC. This makes the tool particularly suitable for system design studies, as the effects of changing system parameters on the system performance can be quickly evaluated. This is a strong benefit of this approach in contrast to e.g. a Computational Fluid Dynamics (CFD) analysis, which may easily occupy several hours for a single run on a similar desktop PC.
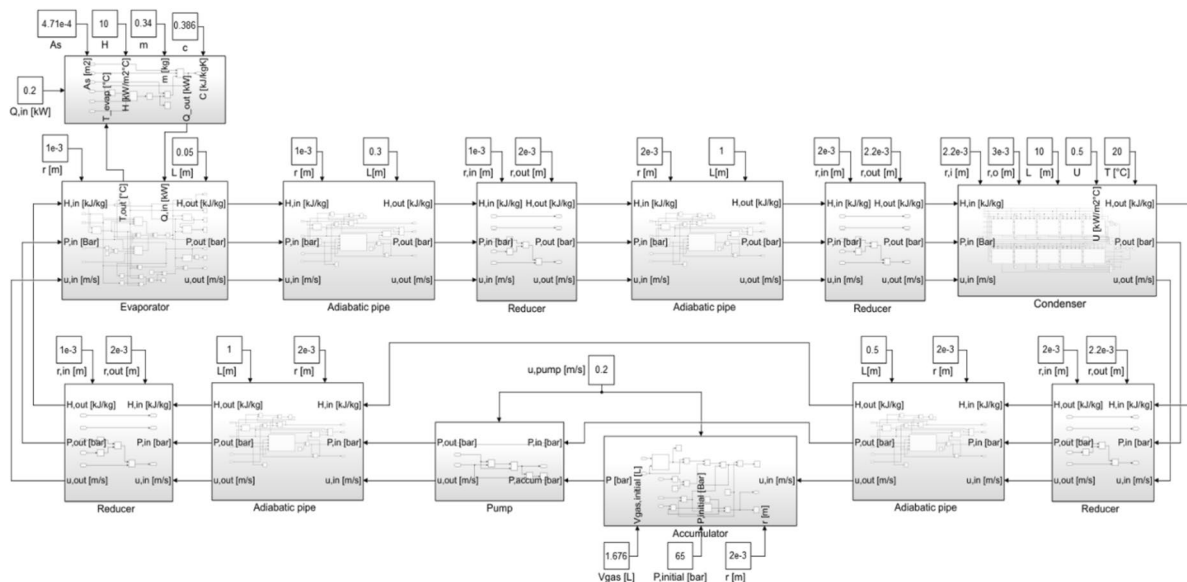
Fig. 6 Developed modular Simulink model for a two-phase pumped loop with, in this case, a single evaporator

4 Prototype setup

A prototype setup of the pumped two-phase cooling system was built and served essentially two purposes. In the first place, it was used to verify the numerical model and to determine if the model is able to accurately predict system performance. Secondly, the prototype helps to determine the practical limits of the system in terms of critical heat flux and dry out. As mentioned, the developed model assumes a constant heat transfer coefficient in the evaporators, regardless of the vapour fraction. Hence, full liquid evaporation would be allowed in the model without the occurrence of dry out. A schematic view of the experimental setup is shown in Fig. 7, in which the locations and corresponding numbers of the applied evaporators, evaporator tubes and sensors are indicated.

For the experiments, the saturation temperature of the CO_2 working fluid was set to 25 °C by controlling the initial accumulator pressure. The maximum working fluid temperature is limited by the CO_2 critical temperature of 31 °C, as was shown in Fig. 2. At this point the fluid will enter a supercritical state and two-phase behaviour will no longer be sustained. At the same time, in order to dispose the heat to a passive condenser, the temperature difference with the environment must be sufficient. For the anticipated heat loads, bringing back the working fluid temperature to 25 °C at the condenser section is possible. To reach a saturation temperature of 25 °C, the initial system pressure must be 65 bar according to the equation of state. During the experiments, the overall system pressure may change when the accumulator absorbs liquid CO_2 to account for fluid expansion in the system.

4.1 System components

Five evaporators are included in the prototype setup, which allow for heat dissipation to the system and mimic electronics components that require active cooling. The evaporators consist of copper blocks in which heat is generated using heating cartridges. The cartridges are cylindrical metal devices that heat up when electrical power is supplied. Power is supplied to the heating cartridges using a variable transformer. The voltage and current are measured by multimeters to accurately determine the power that is supplied to the system. The CO_2 working fluid flows through these blocks in copper tubes with an inner diameter of 2 mm and an outer diameter of 3 mm. All other tubing in the system is made from aluminium and has an inner diameter of 4 mm and outer diameter of 6 mm. For the condenser, a submerged coil heat exchanger is used, in which a 10 mm copper coiled
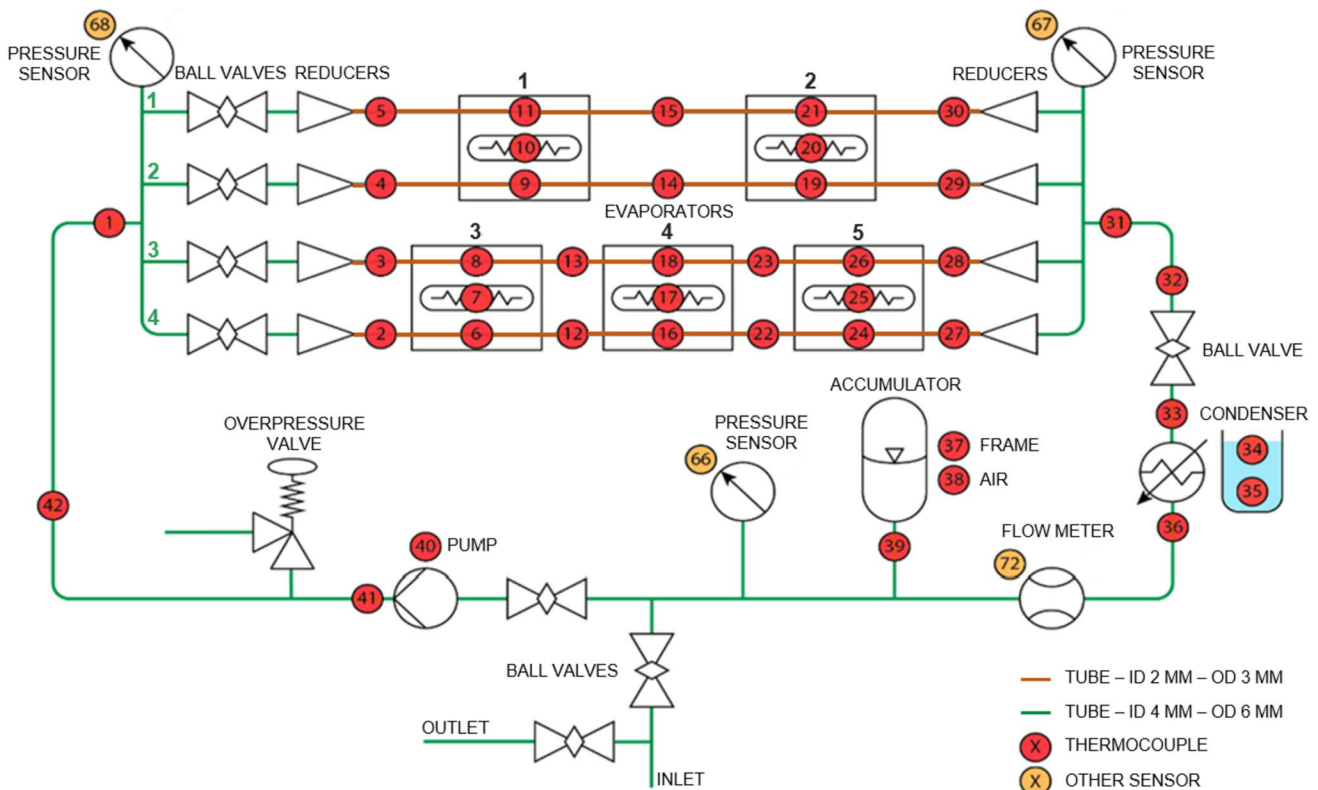

Fig. 7 Schematic overview of the experimental setup including Evaporators 1–5, Evaporator tubes 1–4, and sensor types and locations

brake line is submerged in a vessel with about 60 l of cooling water at 20 °C. Such reservoir is large enough to store the experimental heat loads without significant temperature increase. During off time the reservoir is allowed to cool back to laboratory conditions.

A passive membrane accumulator is used to account for the expansion of the working fluid in the loop. Inside the accumulator a membrane separates inert nitrogen gas at the top section from the CO_2 working fluid at the bottom section. The nitrogen gas is compressed a priori to 60 bar. The accumulator has a total capacity of 2 l, which is sufficient to account for a maximum expected CO_2 inflow of 50 ml during the experiments. This expected inflow is based on a simulation performed with the numerical model, where a total heat input of 600 W was applied to the evaporator. Using the ideal gas law and a maximum desired system pressure of 67 bar, the required accumulator volume was determined to be 2 L. When the system is at its operational pressure, some liquid CO_2 is present in the accumulator. This is required to prevent the membrane from sticking to the accumulator walls. When heat is added to the system and vapour starts to form in the evaporator, liquid-phase CO_2 will be pushed into the accumulator. In that case, the CO_2 working fluid will expand and nitrogen is compressed, which will increase the system pressure moderately.

To continuously propel the working fluid through the loop, a small gear pump is used (TCS Micropumps MGD1000S). The stock version of this micropump has been modified to handle a system pressure up to the critical CO_2 pressure by replacing wetted parts made from plastic by metal equivalents. Since the fluid displacement per pump stroke is small, the gear pump can stably deliver the relatively low flow rates that are required for this application (< 400 ml/min). During operation the energy consumption of the pump is approximately 0.4 W, which is negligible compared to the amount of thermal power that is being transferred.

4.2 Data acquisition

A single variable-area flow meter (KROHNE DK37 M8E) was installed between the condenser and the accumulator. The flow meter, which has a repeatability accuracy of ± 3 ml/min, is used to determine the actual output flow generated by the pump. Furthermore, the flow meter measures the temporary change in flow velocity when the heat load is adjusted to the evaporator(s) due to either fluid expansion or compression. Three IFM pressure transmitters with a range between 0 and 100 bar, and $< 0.5\%$ accuracy were mounted to the setup. The system pressure was recorded before and after the evaporation section, and after the accumulator. The resolution of the pressure sensors is not sufficient to determine local pressure differences due to frictional losses; however, the sensors can accurately determine the system pressure. Finally, in total,

42 T-type thermocouples were mounted on the copper blocks, tubing, accumulator and inside the cooling water and in the ambient air. The thermocouples were calibrated with an initial test, in which the system temperature was logged for several hours at constant temperature. The average value of all thermocouple measurements was used as baseline and the offset for each thermocouple was corrected for during the actual experiments. The thermocouples can measure relative temperature differences with about 0.05 K accuracy. Note that this accuracy is not applicable to the absolute temperature values.

A data acquisition system is used to monitor and record sensor data during the experiments. Next to steady-state results, this gives the opportunity to track the transient behaviour of the system. Due to the limited processing speed of the data acquisition system, data could only be stored every 5 s. An overview of the uncertainties involved with the prototype measurements is given in Table 1. Note that the uncertainty of the derived quantities depends on the actual measured values, since the thermocouples and multimeters provide an absolute accuracy and not a relative value. Following Eqs. 14 and 15, the measurement uncertainty was computed following a standard error analysis method using baseline input values and found to be approximately 5%.

The thermocouple measurements on the evaporator blocks and on the copper tubing connecting these blocks are used to estimate the heat transfer coefficient between the copper blocks and the CO_2 working fluid inside the tubes, based on Eq. 14. In this equation, T_s is the tube's outer surface temperature. For practicality of measurement, T_s is assumed to be equal to the block temperature T_t measured directly above the tube, see Fig. 8. The difference in temperature is deemed insignificant as the offset distance is small, only 3 mm, and the thermal resistance of copper is small compared to the convective thermal resistance inside the tube. T_f is the mean fluid temperature inside the tube. In this case, the average of the incoming T_{in} and outgoing fluid temperature T_{out} for each

Table 1 Uncertainties for measured and derived quantities

Variable	Symbol	Unit	Uncertainty
Measured quantities			
Temperature	T	[K]	± 0.05 K
Pressure	P	[Pa]	$< 0.5\%$
Flow rate	V	[L/min]	± 3 ml/min
Voltage	U	[V]	0.1 V
Current	I	[A]	0.01 A
Derived quantities			
Heat transfer coefficient	h	[W/m²K]	*Following Eq. 14, appr. 5%*
Heat flux	q''	[W/m²]	*Following Eq. 15, appr. 5%*
Heat input	q	[W]	*Following $q = U \cdot I$, appr. 1%*
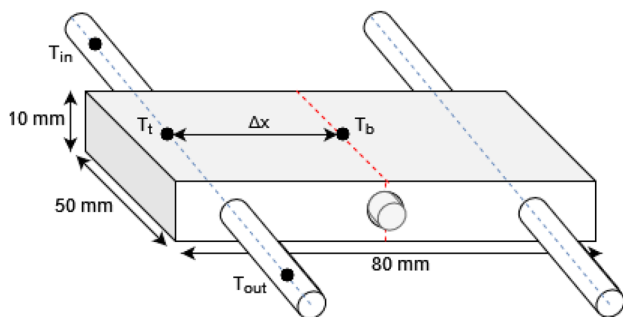
Fig. 8 Measured parameters to determine the heat transfer coefficient of the evaporators

block is taken as the mean fluid temperature. As one heating cartridge was used for heating two tubes, the individual contribution to each tube was determined by computing the heat flux q'' according to Eq. 14. Here, ΔT is the temperature difference between the middle of the block T_b and the location above the tube T_t, and Δx is the distance between the thermocouples at these locations. The parameters involved in Eqs. 14 and 15 are schematically indicated in Fig. 8.

For the experimental analysis, the measured heat transfer coefficient h will be used to determined system performance, identify dry out and to compare results with other pumped two-phase loop experiments in literature. Furthermore, the heat transfer coefficient is required to determine the heat input at the evaporator in the numerical model, Q_{in} of Eq. 8. As the developed model uses a modular evaporator with one thermal mass and heat input, the heat transfer coefficient should be based on a mean evaporator temperature. The measured heat transfer coefficient, based on Eq. 14, however uses the temperature T_t just above the tube. Herewith the heat transfer coefficient is slightly overestimated; however, other empirical relations from literature are known to be 30% off [37]. The advantage is this approach is that measured values can be better compared to literature sources without having to compensate for the evaporator block design.

$$h = \frac{q\varepsilon}{T_s - T_f} \approx \frac{q\varepsilon}{T_t - \frac{T_{in}+T_{out}}{2}} \tag{14}$$

$$q\varepsilon = -k\frac{\Delta T}{\Delta x} \approx -k\frac{T_b - T_t}{\Delta x} \tag{15}$$

5 Results

The experiments performed with the prototype setup were aimed to identify the system's limits, i.e. how much heat the system could dissipate and with what evaporator configuration dry out occurs first. Furthermore, a comparison
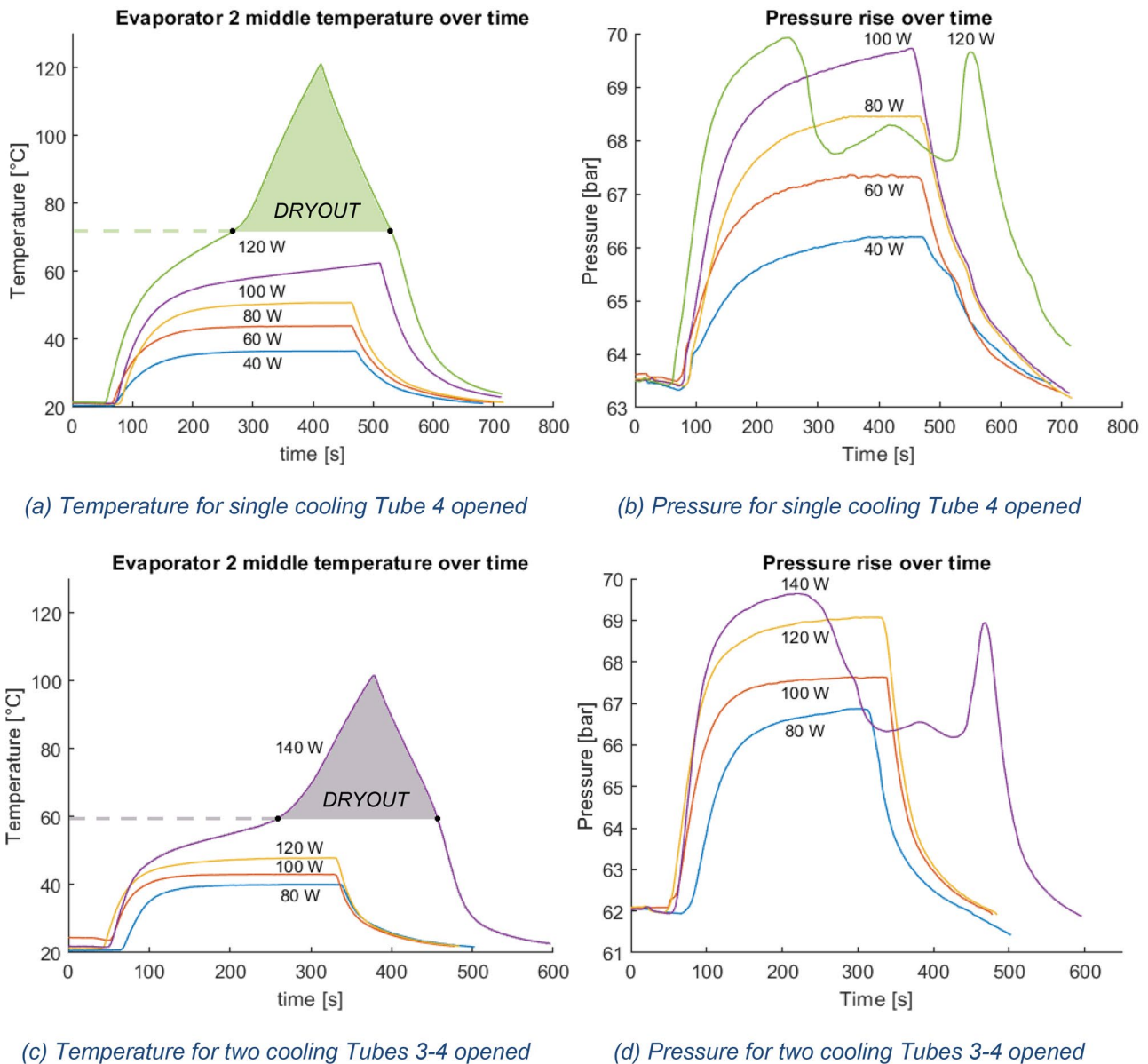
between predictions of the numerical model and experimental results is made to validate model accuracy. The occurrence of dry out is investigated for a fixed flow rate of the working fluid with increasing heat load on the evaporator section. The comparison with the numerical model is made by comparing evaporator block temperatures, system pressure and flow velocity after the condenser section.

5.1 Dry out

To determine the operating range of the prototype setup in terms of heat input, tests with gradually increasing heat load were performed. The flow rate was kept constant at 300 ml/min and the heat load was applied to Evaporator 4 only (see Fig. 7). This round of experiments consisted of two sets. In the first set, a single evaporator channel (Tube 4) was opened while in the second set both evaporator channels (Tubes 3–4) were opened. The latter allows the working fluid to flow through both tubes simultaneously, thereby increasing the heat transfer area and decreasing the net heat flux per tube. The heat input is limited by the critical heat flux and critical vapour fraction. When the critical heat flux or critical vapour fraction is reached, dry out takes place and the temperature of the evaporator block will rise rapidly.

The results for the experiments in which a single evaporator channel was opened are shown in Fig. 9(a,b). The evaporator temperature is evaluated at the middle of Evaporator 4 (T_b according to Fig. 8) and the pressure data is obtained near the accumulator with pressure sensor 66 in Fig. 7. For the lower heat inputs (< 100 W), the temperature and pressure increase rapidly when the heat load is turned on and reach an equilibrium value. As expected, the higher the heat input, the higher the equilibrium temperature and pressure. Since a higher fraction of the working fluid evaporates with higher heat inputs, more vapour is formed in the system and the amount of liquid CO_2 flowing into the accumulator increases, resulting in a higher system pressure. When two evaporator channels were opened, more heat could be added to the system before dry out occurred, as shown in Fig. 9(c,d).

For both sets of experiments, the same dry-out behaviour could be observed at the maximum heat load. In this dry-out region, indicted by the shaded triangle in Fig. 9(a, c), the slope of the curve changes significantly at the dashed horizontal line, indicating that a transition in flow regime has taken place. At the peak of the triangle the heat load was switched off and the system was allowed to stabilize. Figure 9(b, d) illustrate the system pressure for both test sets. During dry-out conditions, the pressure quickly drops, since vapour patches near the tube walls isolate the bulk fluid and prevent proper heat transfer

(a) Temperature for single cooling Tube 4 opened

(b) Pressure for single cooling Tube 4 opened

(c) Temperature for two cooling Tubes 3-4 opened

(d) Pressure for two cooling Tubes 3-4 opened

Fig. 9 Effect of increasing heat input on evaporator temperature and pressure with constant flow rate

from the wall to the fluid. This results in less overall fluid expansion and hence a lower system pressure. At load off, a small temporary pressure increase is recorded. At the lower right corner of the shaded triangle, again the slope of the temperature curve changes and also the pressure rises to its original value. This rise in pressure corresponds to the point where the flow wets the tube wall again and the original flow regime is restored. This is confirmed by the last part of the temperature curve after the shaded triangle, where the cool-down behaviour is similar to the other experiments where dry out did not occur. The distinct w-shaped transient response of the pressure during dry out was witnessed in all dry-out experiments. Similar

to the reported oscillation by [24, 25], such behaviour occurs at load-on and load-off conditions as well as shifts in flow regime.

The transition in flow regime happens around the same evaporator block temperature for both heating up and cooling down. As the heat flux from the evaporator block to the working fluid is related to the temperature difference between the block and the tube according to Eq. 14, the critical heat flux was reached at the transition temperature. In the first set of experiments the critical evaporator block temperature is 72 °C, while in the second set of experiments the critical heat flux is obtained at a block temperature of 59 °C. When both channels are opened, the mass flow rate

per channel is lower, resulting in a higher vapour fraction after the evaporator compared to the experiments in which a single channel was opened. Since the critical heat flux decreases with increasing vapour fraction [43], dry out occurred at a total heat load of about 140 W (70 W per channel), while for a single channel the critical heat flux is obtained at a heat load around 100 W.

5.2 Heat transfer coefficient

In Fig. 10, the effect of increasing the heat load on the heat transfer coefficient is shown for the experiments in which a stable equilibrium temperature was achieved at the evaporator (see Fig. 9). When a single evaporator channel is opened, Fig. 10(a) shows a steady increase in heat transfer coefficient with increasing heat load for Tube 4. This matches the theory of boiling flow, in which increasing the heat flux results in a higher heat transfer coefficient due to the enhancement of nucleate boiling [43]. Tube 3, which was closed, showed some heat losses due to conduction through the tube wall. As heat transfer to the fluid improves for higher heat loads, the heat transfer loss to the closed Tube 3 diminishes. In the tests where both evaporator channels were opened, the heat transfer coefficient drops when increasing the heat load from 100 to 120 W, as shown in Fig. 10(b). This could indicate the onset of dry out, as local vapour patches are being formed at the tube wall that start to isolate the liquid core and decrease the heat transfer rate. As was shown in Fig. 9(c,d), the next heat load setting after 120 W resulted in dry out of the evaporator.

Delil et al. [16] and Pettersen et al. [44] investigated heat transfer characteristics for evaporating CO_2 at similar conditions and found heat transfer coefficients in the range of 5 to 15 kW/(m^2K), hence the obtained values match the expected range very well. Assuming that both tubes should perform equally good, the measured differences in heat transfer coefficient is also a measure for the system accuracy. The

average error between both tubes is just below 10%. Hence, next to the measured accuracy of 5%, also a small systematic bias is present related to the prototype set-up itself.

5.3 Model comparison

In order to make a comparison with the predicted values of the numerical model, measurements obtained with the sensors of the prototype setup have been used. Firstly, the temperature of the evaporator block is compared to the model when 60 W is applied on a single evaporator block cooled by one channel, Tube 4. In the model, the evaporator block is modelled as a thermal mass with a single temperature. A constant heat transfer coefficient of 10 kW/m^2K is applied to the evaporator, which corresponds to the results found for the single evaporator experiment, see Fig. 10(a). To compare the prototype results with the model, the temperature measured at the top of the evaporator block are averaged with the temperature measured at the middle of the block (T_t and T_b, respectively, in Fig. 8). Figure 11 shows the transient temperature profile when a 60 W heat load was applied for approximately 300 s at time t = 160 s. The pump speed was set to provide a constant working fluid flow rate of 300 ml/min during the experiment.

The figure shows that both the shape and numerical values of the temperature profile match very well. The first part of the curve, when heating up, correlates perfectly. This indicates that the heat transfer coefficient between the working fluid and the evaporator during heating has been matched well and the thermal mass of the evaporator corresponds to the actual value. After the heat load is turned off, the prototype cools down less rapidly. This is due to the fact that in reality the heat transfer coefficient declines when the heat flux decreases during cooling. In the model the heat transfer coefficient at the evaporator is assumed to be constant, which results in faster cooling of the thermal mass element.

The temperature of the CO_2 working fluid in the opened cooling channel after the evaporator block (sensor #22 in Fig. 7)

Fig. 10 Heat transfer coefficients for varying heat input

(a) One evaporator channel (Tube 4) opened

*(b) Two evaporator channels (Tubes 3-4) opened*
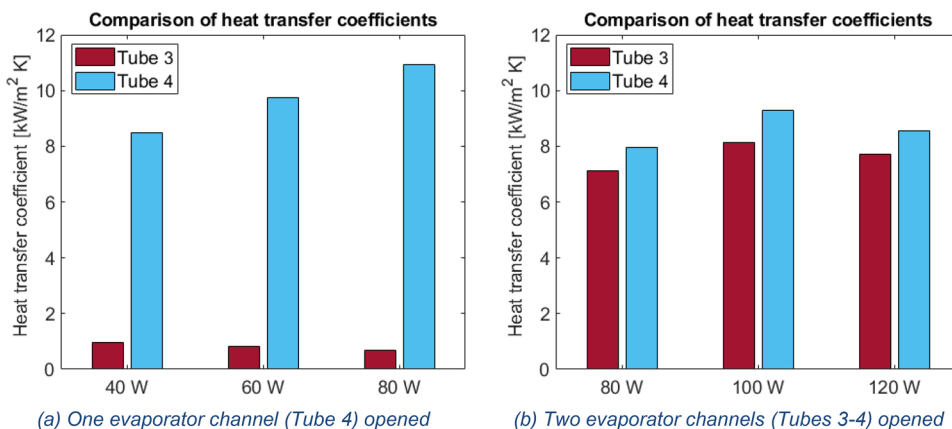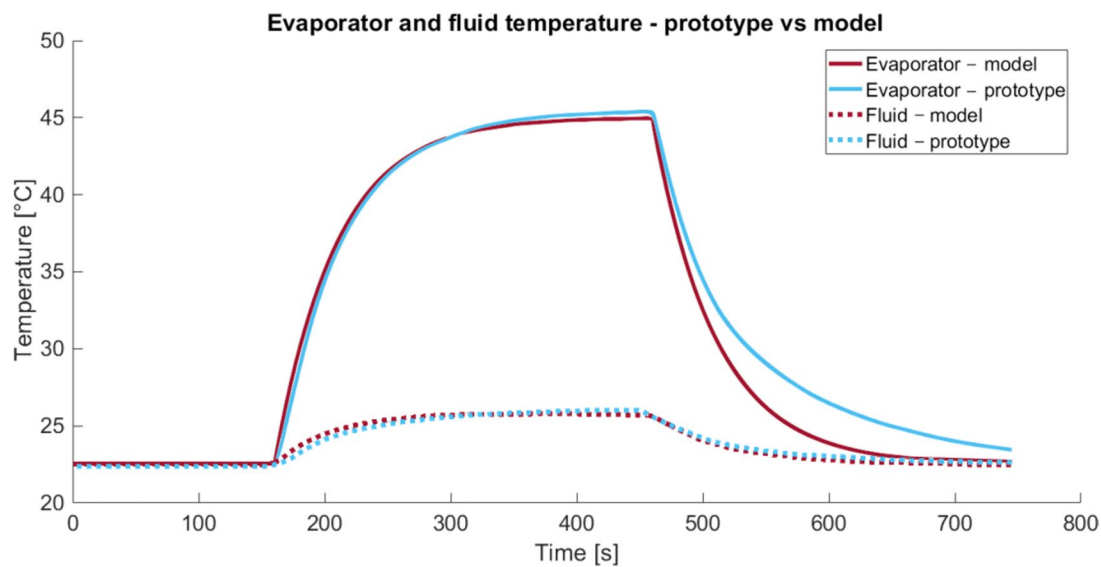
Fig. 11 Evaporator temperature with 60 W applied to an evaporator with a single Tube 5 opened

is compared with the corresponding fluid temperature from the numerical model as well. Also, in this case, both profiles are a close match. The temperature of the working fluid rises due to heat absorption until the saturation temperature is reached. Further heat absorption takes place by evaporation and therefore the temperature stabilizes. During the evaporation process, vapour starts to form in the evaporator channel. Since the vapour density is much lower than the liquid density, expansion takes place and the flow velocity in the system increases. Vapour expansion continues until the two-phase flow reaches the condenser section where the vapour is condensed to liquid

again. The temporary peak in flow velocity, as discussed in Fig. 1, is predicted by the numerical model and was also measured by the flow meter in the prototype setup.

Figure 12 compares the predicted flow rate after the condenser section with the measured values of the variable area flow meter. Fluctuations are present in the measured values due to the data acquisition system which only stored data every 5 s. Furthermore, the repeatability accuracy of the flow meter is limited to ± 3 ml/min. Although this error margin is larger than the observed trend in Fig. 12, the expected behaviour was observed.
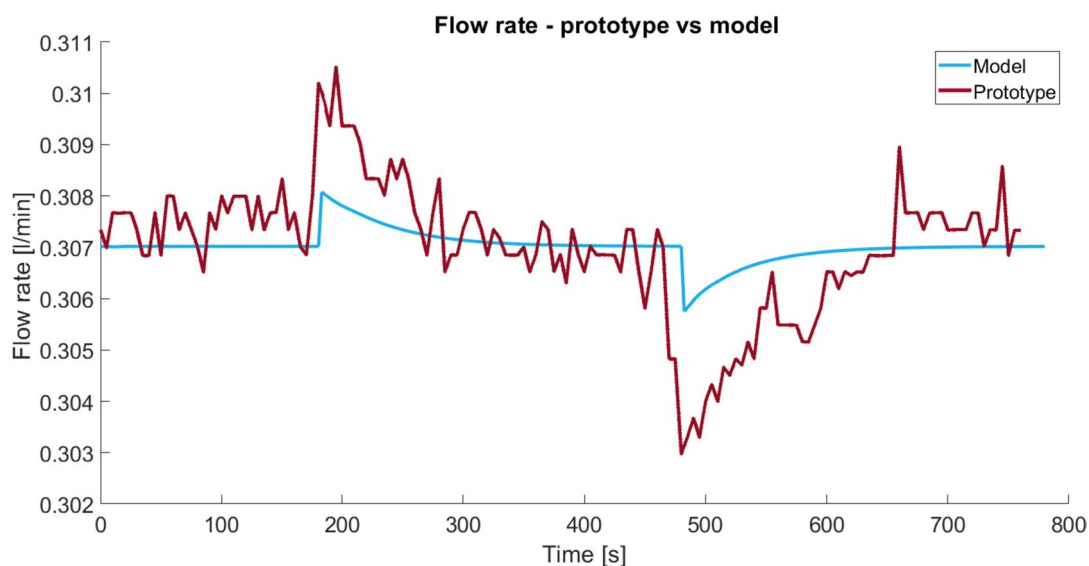
Fig. 12 Flow rate with 60 W applied to an evaporator with a single Tube 4 opened

The general shapes of the curves match, yet the measured peak values are about four times higher compared to the predicted results. Hence, more vapour is formed in the actual evaporator than predicted by the numerical model. This can be explained by the fact that the numerical model assumes one dimensional flow, in which subcooled boiling near the channel walls is not included. In the model, vapour formation is only predicted when the working fluid has fully reached its saturation temperature. For the prototype setup, local boiling can occur near the channel walls while the bulk fluid is still in the subcooled regime. Due to the relatively large difference in density between the liquid and vapour phases, localized subcooled boiling increases the total amount of expansion significantly. Additionally, the estimated heat transfer coefficient at the condenser coil can be lower in reality, causing more vapour to sustain in the condenser spiral. This would increase the total amount of vapour in the system and could therefore also contribute to the observed flow velocity behaviour.

The excess volume present in the system when the evaporator is active is absorbed by the accumulator. When the net flow velocity after the condenser is greater than the steady-state value set by the gear pump, liquid is absorbed by the accumulator. For a passive membrane accumulator, this means the pressure in the system will rise, as the gas in the top section is being compressed. Therefore, liquid absorption by the accumulator results in a direct increase in system pressure. This is shown in Fig. 13, in which the pressure rise of the prototype setup is compared with the predicted increase in pressure by the numerical model. Since the pressure rise is a direct result of the increase in flow velocity, the absolute values are underestimated as well. However, the general shape of the curve is correct. Furthermore, when the accumulator inflow is simulated to be four times as large in the numerical model, to mimic the actual system behaviour of Fig. 12, the pressure would rise to the measured level of 68.17 bar. This suggests that the physical principles that govern the numerical model are correctly implemented.

5.4 Multiple evaporators

The effects of applying a heat load on multiple evaporators simultaneously has also been investigated using the prototype setup. Here, the advantage of the modular numerical model can be utilized. An experimental set was conducted in which all 4 cooling channels of the evaporator section were opened and the total heat load was equally distributed over Evaporators 1, 2, 4 and 5, see Fig. 7. The total heat input was increased per experimental run from 80 to 320 W; i.e. 20 W to 80 W per evaporator block.

In Fig. 14 the heat transfer coefficients of Tubes 3 and 4 measured at Evaporator 4 are shown for an increasing heat input. Similar to the results obtained for the single evaporator experiment, increasing the heat load on the evaporator results in a higher heat transfer coefficient, up until the point where dry out starts to occur. In this case, Evaporator 4 starts to experience dry out at a local heat load of 80 W and a slight decline in heat transfer coefficient is witnessed.

Similarly, in Fig. 15, the heat transfer coefficients measured at Evaporator 5 are shown for the same set of experiments. At the lowest total heat input of 80 W, the measured heat transfer coefficient is nearly 6 kW/m^{2}K, while the heat transfer coefficient at Evaporator 4 in this case is less than 4 kW/m^{2}K. For a total heat input up to 240 W, Evaporator
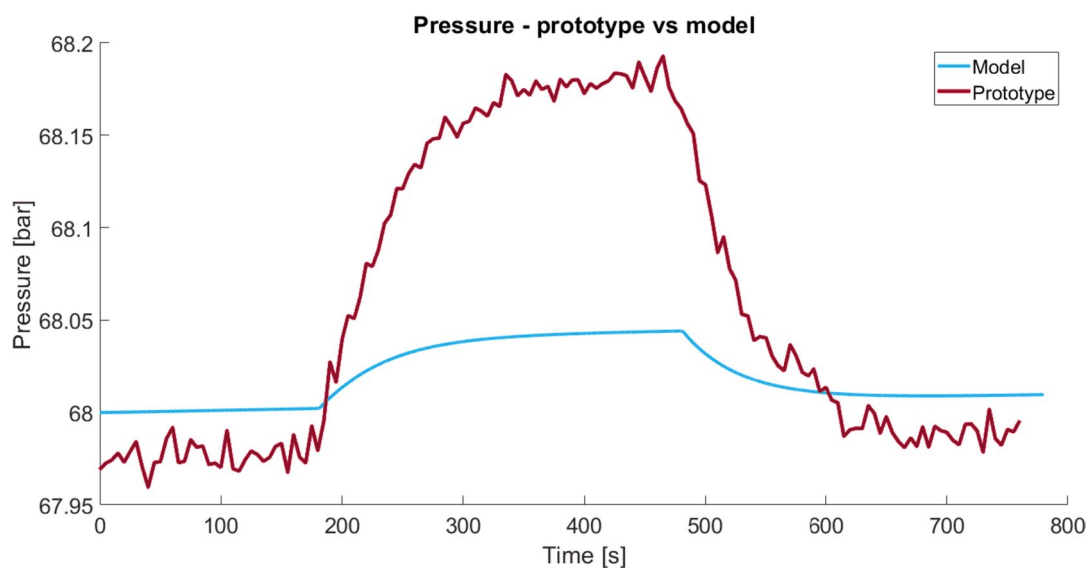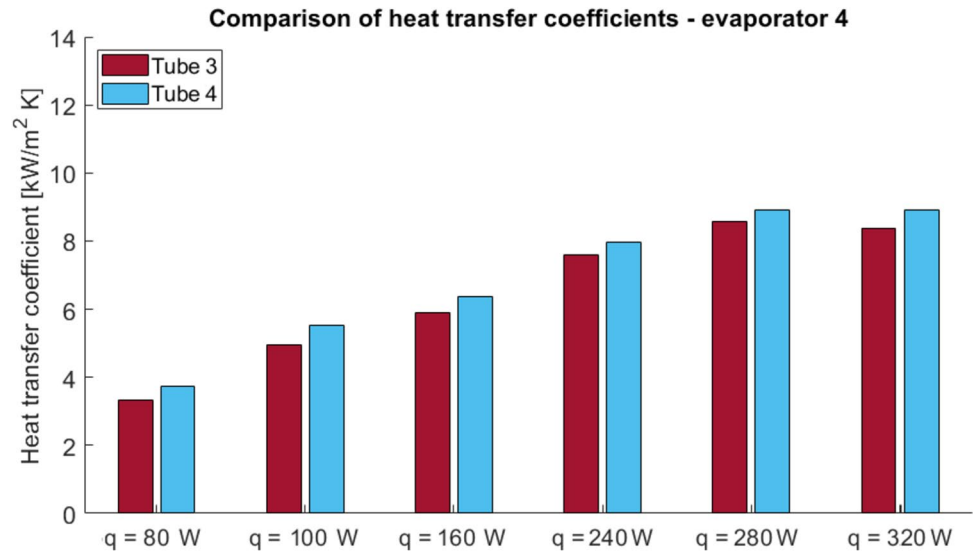

Fig. 13 System pressure with 60 W applied to an evaporator with a single Tube 4 opened

Fig. 14 Heat transfer coefficient for different head loads on Evaporator 4


5 consistently shows higher heat transfer coefficients. However, dry out starts to occur at a total heat input of 280 W for Evaporator 5, while for Evaporator 4 this was not experienced until 320 W.

Both observations can be explained by the occurrence of pre-heating. Liquid CO_2 enters the evaporator section in the subcooled state. When the working fluid arrives at Evaporators 1 and 4, heat is initially absorbed as sensible heat and boiling only occurs locally near the channel walls. When the bulk fluid has reached the saturation temperature, full flow boiling takes place. This is the case at Evaporators 2 and 5, as the incoming working fluid is already pre-heated to the saturation temperature by Evaporators 1 and 4. Since flow boiling results in higher heat transfer rates when compared to single-phase forced convection [33], higher heat transfer coefficients are obtained at Evaporator 5 compared

to Evaporator 4. However, dry out is experienced earlier due to the higher vapour fraction, which limits the critical heat flux. At a total heat input of 320 W, Evaporator 5 exhibits full dry out in which hardly any heat is transferred to the working fluid resulting in a large drop in heat transfer coefficient.

The effect of pre-heating is further investigated in Fig. 16, in which the heat transfer coefficients of the four evaporator blocks are shown for a total heat input of 240 W and 320 W respectively. Figure 16(a) shows that heat transfer coefficients are higher at Evaporators 2 and 5 due to pre-heating. When a total heat load of 320 W is applied however dry out occurs at Evaporators 2 and 5 and the heat transfer coefficients decline significantly, as witnessed in Fig. 16(b). Note that with a total heat load of 80 W per evaporator block, dry out occurred sooner than for the single

Fig. 15 Heat transfer coefficient for different heat loads on Evaporator 5
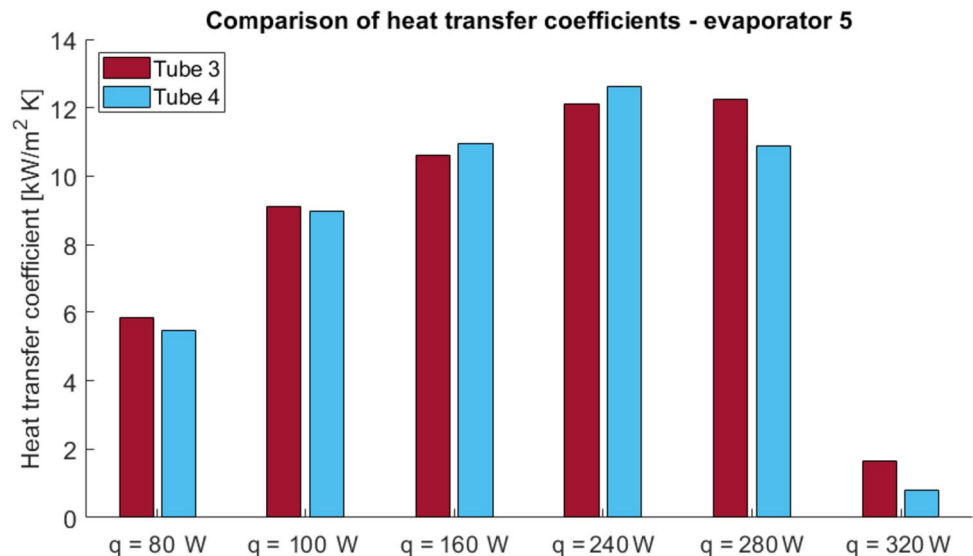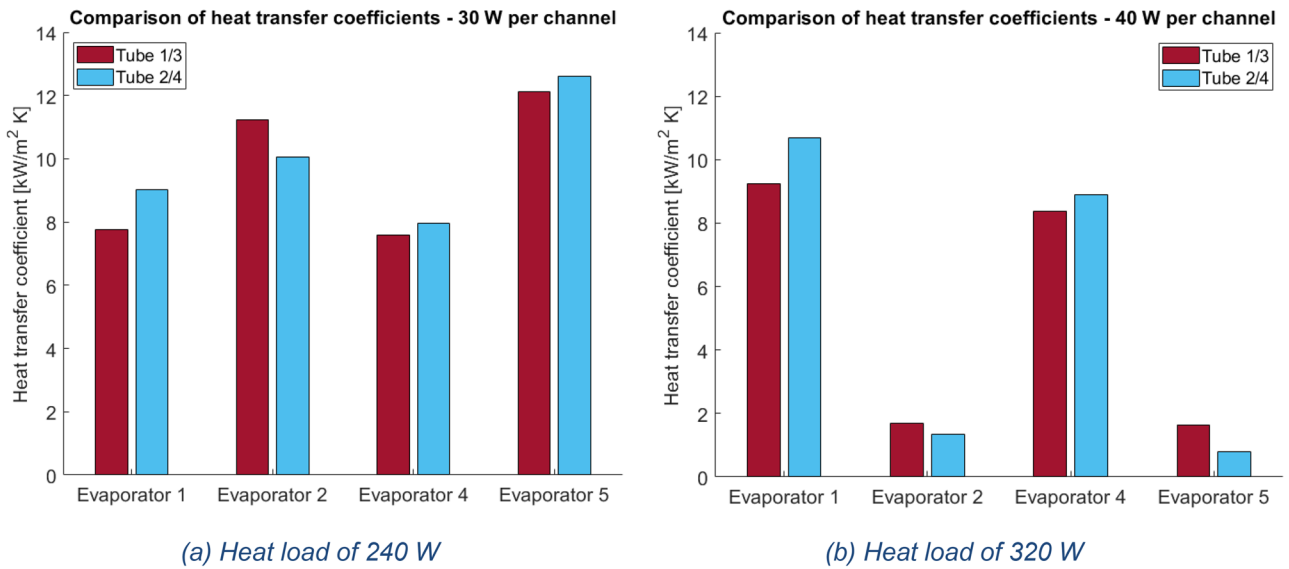
Fig. 16 Heat transfer coefficients for different evaporators and increasing heat load

evaporator experiments. With two cooling channels (Tubes 3–4) opened, dry out took place when more than 120 W was applied to a single evaporator block, see Fig. 9(c). When multiple evaporators are used and all cooling channels of the setup are open, the total flow rate per tube is lower. Hence, the critical vapour quality is reached earlier, resulting in dry out at a lower heat input per block.

For the multiple evaporators experiment in which a total heat load of 240 W is applied, again a comparison with the numerical model is made. In Fig. 17, the temperature of

Evaporators 1 and 2 is investigated. Heat transfer coefficients of 8 and 10 kW/m^{2}K were used for these evaporators, respectively, corresponding to the values determined as presented in Fig. 16(a). Due to the difference in heat transfer coefficient, Evaporator 2 stabilizes at a slightly lower temperature than Evaporator 1.

Similar to the single evaporator comparison of Fig. 11, the numerical model and prototype results correlate very well for the first part of the curves, during heating up and at steady-state conditions. After the heat load is turned off,
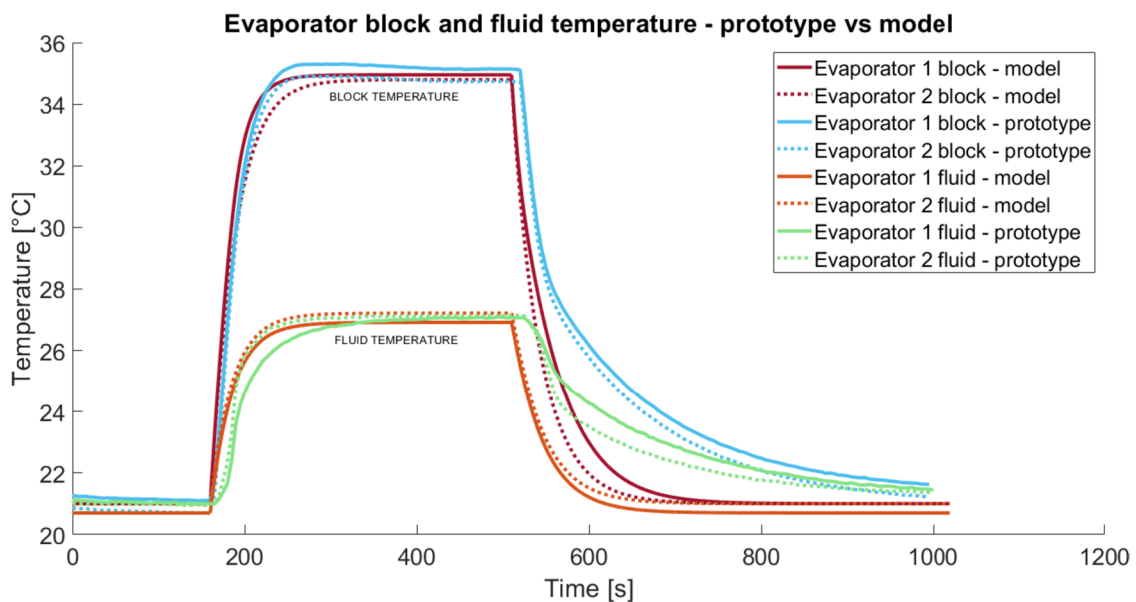
Fig. 17 Temperature for Evaporators 1 and 2 with a total heat load of 240 W applied

Flow rate - prototype vs model
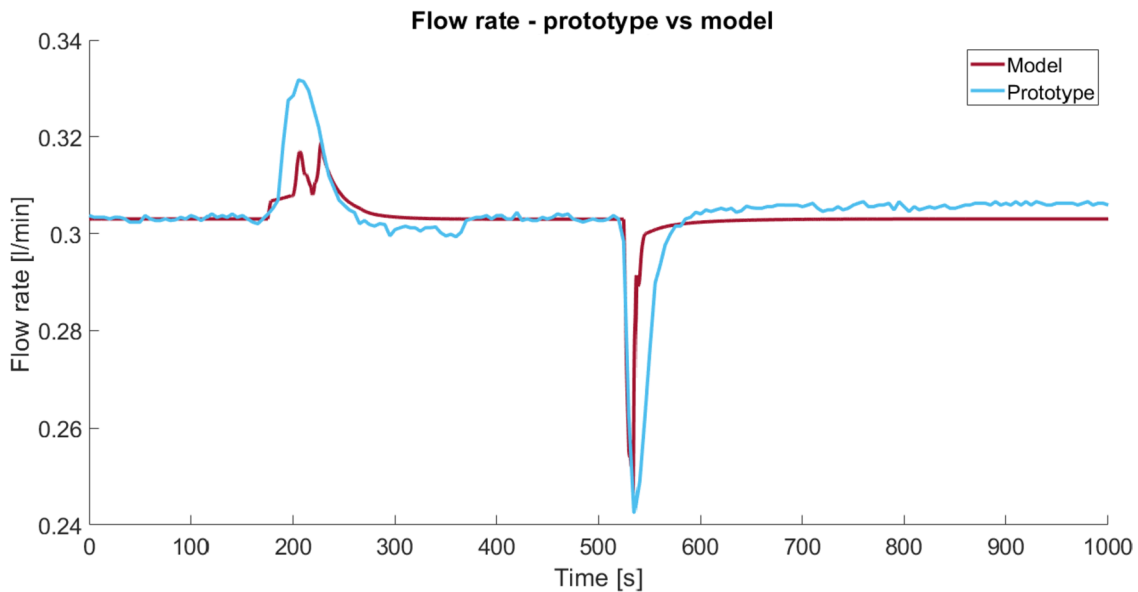
Fig. 18 Flow rate with 240 W distributed over 4 evaporators with all tubes opened

the prototype cools down less rapidly than the numerical model predicts, due to the assumption of a constant heat transfer coefficient in the numerical model. Also, the fluid temperatures compare well.

The flow rate measured with the variable area flow meter of the prototype setup is compared with the numerical model and shown in Fig. 18. The temporary peaks in flow rate after the heat load is switched on and switched off are clearly present.

In this case, the peak values are more than 10 times higher than the repeatability accuracy of the flow meter, due to the much higher total heat load. Hence, the observed

profile appears smoother. Again, the numerical model underestimates the amount of fluid expansion, resulting in lower predicted peak values. As two evaporators are placed in series and the model uses two constant, yet different heat transfer coefficients for each evaporator, vapour formation is initiated at two distinct time instances. This causes two separate vapour expansion characteristics resulting in the prediction of two distinct peaks in the flow rate between 200 and 250 s. As in the experiment, the heat transfer coefficient is not constant, but a consequence of the local flow behaviour, the measured flow rate shows a smoother single

Pressure - prototype vs model
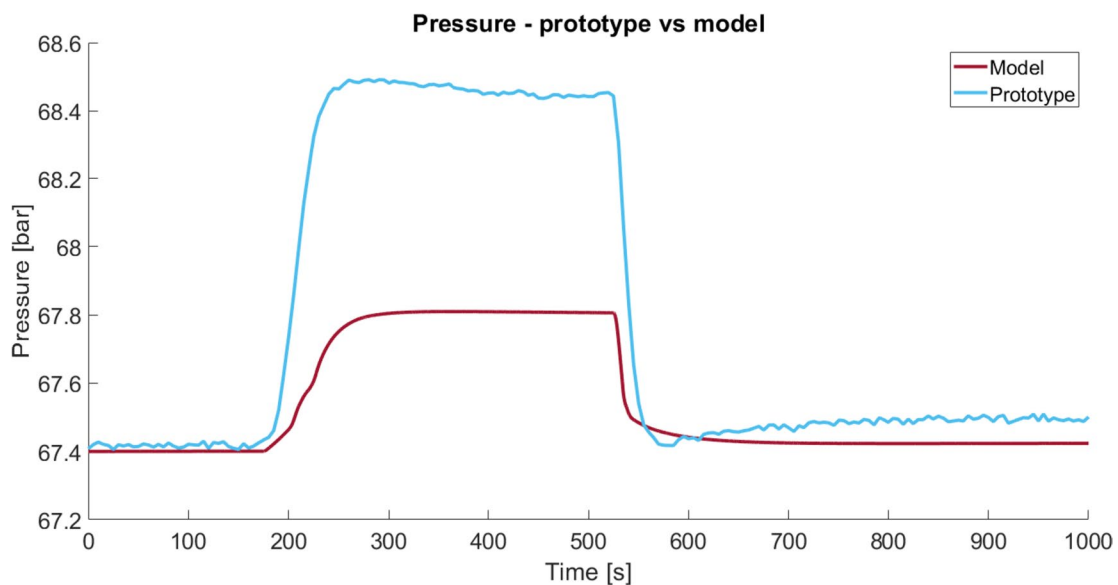
Fig. 19 System pressure with 240 W distributed over 4 evaporators with all tubes opened

peak. Altogether, similar to the single evaporator experiment of Fig. 12, also for multiple evaporators in parallel and in series, the model is able to capture the governing physical principles.

The system pressure measured during the parallel evaporator experiment with a total heat load of 240 W is compared with the numerical results and shown in Fig. 19. As the system pressure is directly correlated to the accumulator inflow, the pressure follows the trend of the flow rate shown in Fig. 18. Due to the fact that the peaks in flow velocity develop later in the numerical model, the increase in pressure also lags behind when compared to the prototype measurements. However, also in this case the model is capable of representing the underlying physical principles of the pumped two-phase loop.

6 Conclusions

Pumped two-phase systems may offer a solution to efficiently cool high power-density systems. However, the physics of flow boiling are complicated and the performance of a pumped two-phase loop depends on many system parameters. To address these issues, the numerical and experimental work presented in this paper was performed. The main findings are:

- A graphical modelling approach was used to build a fast and convenient design tool for predicting two-phase system behaviour based on the integral forms of the mass, momentum and energy conservation equations.
- A prototype setup for a pumped two-phase loop using carbon dioxide (CO_2) as working fluid was built to investigate system performances and practical operational limits. Temperature, flow and pressure data are measured during the experiments to monitor the system state and to validate the developed numerical model.
- Experiments performed with the prototype setup showed an increase in heat transfer coefficient with increasing heat load until dry out starts to occur. Heat transfer coefficients between 7 and 10 kW/m^{2}K were found, which is comparable to other experiments conducted with evaporating CO_2 in microchannels.
- When the heat flux surpasses its critical value, dry out occurs in the microchannels and the evaporator temperature rises significantly. Similar behaviour was found when multiple evaporators were heated in series and/or in parallel.
- Comparing the numerical model to the prototype setup, it was shown that evaporator and working fluid temperatures can be predicted accurately. Pressure and flow measurements were in agreement with the model in a qualitative manner. However, the measured peak values

are consistently underestimated, due to the assumption of one-dimensional flow boiling and neglecting subcooled boiling at the evaporator wall in the numerical model.
- Due to its modular approach, the presented model is particularly useful for the rapid assessment of various layouts of pumped two-phase loops for high heat flux electronics cooling.

In future work, the numerical model may be compared more extensively with additional experimental datasets, focussing on evaporator inflow and system pressure. Preheating can be applied to make the working fluid enter the evaporator section in saturated state, eliminating the effect of subcooled nucleate boiling. As boiling would occur more homogenous, a closer match with the numerical model is expected.

Declarations

References

1. Moore GE (1965) Cramming more components onto integrated circuits. McGraw-Hill New York
2. Zhang Z, Wang X, Yan Y (2021) A review of the state-of-the-art in electronic cooling. E-Prime Adv Electr Eng Electron Energy 1:100009. https://doi.org/10.1016/j.prime.2021.100009
3. Wang CC (2017) A Quick Overview of Compact Air-Cooled Heat Sinks Applicable for Electronic Cooling—Recent Progress. Inventions 2(1). https://doi.org/10.3390/inventions2010005
4. McGlen RJ, Jachuck R, Lin S (2004) Integrated thermal management techniques for high power electronic devices. Appl Therm Eng 24(8):1143–1156. https://doi.org/10.1016/j.applthermaleng.2003.12.029
5. Hoang CH et al (2021) A Review of Recent Developments in Pumped Two-Phase Cooling Technologies for Electronic Devices. IEEE Trans Compon Packag Manuf Technol 11(10):1565–1582. https://doi.org/10.1109/TCPMT.2021.3117572
6. Sharar D, Jankowski NR, Morgan B (2010) Review of two-phase electronics cooling for army vehicle applications

7. Faghri A (2014) Heat pipes: Review, opportunities and challenges. Front Heat Pipes 5. https://doi.org/10.5098/fhp.5.1

8. Wits WW, Kok JB (2011) Modeling and validating the transient behavior of flat miniature heat pipes manufactured in multilayer printed circuit board technology. J Heat Transf 133(8). https://doi.org/10.1115/1.4003709

9. Wits WW, Te Riele GJ (2019) Heat Pipe Array for Planar Cooling of Rotating Radar Systems. J Heat Transf 141(9). https://doi.org/10.1115/1.4043183

10. Wang ZR et al (2017) Design and performance of a mechanically pumped two-phase loop to support the evaporation-condensation experiments on the TZ1. Case Stud Therm Eng 10:650–655. https://doi.org/10.1016/j.csite.2017.11.008

11. Delil AA (2004) Current Mechanically Pumped Two-Phase Thermal Control Loop Developments. SAE International, Warrendale, PA, SAE Technical Paper 2004-01-2507. https://doi.org/10.4271/2004-01-2507

12. Gorbenko G, Gakal P, Turna R, Hodunov A (2021) Retrospective Review of a Two-Phase Mechanically Pumped Loop for Spacecraft Thermal Control Systems. J Mech Eng 24:27–37. https://doi.org/10.15407/pmach2021.04.027

13. Oren JA (1981) Study of thermal management for space platform applications: Unmanned modular thermal management and radiator technologies. REPT-2-53020/1R-52778. Accessed 25 Oct 2022. [Online]. Available: https://ntrs.nasa.gov/citations/19810020609

14. Holloway PF (1982) Space station technology. Paris Int Astronaut Fed Congr. Accessed 25 Oct 2022. [Online]. Available: https://ui.adsabs.harvard.edu/abs/1982pari.iafcX....H

15. Bednov SM et al (2003) Perspective thermal control systems (TCS) of spacecrafts on the basis of two-phase mechanical pumping loops. Proc 5th Int Seminar on Heat Pipes, Heat Pumps and Refrigerators, Minsk, Belarus

16. Delil AA, Woering AA, Verlaat B (2002) Development of a mechanically pumped two-phase CO2 cooling loop for the AMS-2 tracker experiment

17. Verlaat B, Van Beuzekom M, Van Lysebetten A (2008) CO2 cooling for HEP experiments. Proc. Topical Workshop on Electronics for Particle Physics, pp 328–336. https://doi.org/10.5170/CERN-2008-008.328

18. Es JV, Van Gerner HJ (2013) Benefits and drawbacks of using two-phase cooling technologies in military platforms. Electron Cool Spring Issue

19. Kelkar KM, Patankar SV, Kang SS, Iyengar M, Schmidt RR (2010) Computational method for generalized analysis of pumped two-phase cooling systems and its application to a system used in data-center environments. 2010 12th IEEE Intersociety Conference on Thermal and Thermomechanical Phenomena in Electronic Systems, IEEE, pp 1–11

20. Zhang P, Wei X, Yan L, Xu H, Yang T (2019) Review of recent developments on pump-assisted two-phase flow cooling technology. Appl Therm Eng 150:811–823. https://doi.org/10.1016/j.applthermaleng.2018.12.169

21. van Gerner HJ, Braaksma N (2016) Transient modelling of pumped two-phase cooling systems: Comparison between experiment and simulation. Accessed 18 Sep 2022. [Online]. Available: https://ttu-ir.tdl.org/handle/2346/67471

22. Jie L, Nian-Qiang P, Kai-Hua G, Zhen-Hui H, Ting-Xuen L (2008) Experimental investigation on a mechanically pumped two-phase cooling loop with dual-evaporator. Int J Refrig 31(7):1176–1182. https://doi.org/10.1016/j.ijrefrig.2008.02.014

23. Lee M, Park C (2018) Mechanical-capillary-driven two-phase loop: Numerical modeling and experimental validation. Int J Heat Mass Transf 125:972–982. https://doi.org/10.1016/j.ijheatmasstransfer.2018.04.144

24. Meng Q et al (2020) Experimental study on the transient behaviors of mechanically pumped two-phase loop with a novel accumulator for thermal control of space camera payload. Appl Therm Eng 179:115714. https://doi.org/10.1016/j.applthermaleng.2020.115714

25. Li L, Tao J, Gao W (2021) Experimental Study on the Dynamic Heat Transfer Characteristics of a Mechanically Pumped Two-phase Cooling Loop. Front Energy Res 9. Accessed 18 Sep 2022. [Online]. Available: https://www.frontiersin.org/articles/10.3389/fenrg.2021.701805

26. Bolder R (2017) Numerical Simulation of a Two-Phase Thermal Control System. Accessed 18 Sep 2022. [Online]. Available: https://repository.tudelft.nl/islandora/object/uuid%3A5c1f3e42-cdeb-47c7-9e7f-0ffba799b3f9

27. van Gerner HJ, Van Benthem RC, Es JV, Schwaller D, Lapensée S (2014) Fluid selection for space thermal control systems. 44th International Conference on Environmental Systems. Accessed 18 Sep 2022. [Online]. Available: https://ttu-ir.tdl.org/handle/2346/59591

28. Cheng L, Xia G, Thome JR (2021) Flow boiling heat transfer and two-phase flow phenomena of CO2 in macro- and microchannel evaporators: Fundamentals, applications and engineering design. Appl Therm Eng 195:117070. https://doi.org/10.1016/j.applthermaleng.2021.117070

29. Karayiannis TG, Mahmoud MM (2017) Flow boiling in microchannels: Fundamentals and applications. Appl Therm Eng 115:1372–1397. https://doi.org/10.1016/j.applthermaleng.2016.08.063

30. Kew PA, Cornwell K (1997) Correlations for the prediction of boiling heat transfer in small-diameter channels. Appl Therm Eng 17(8):705–715. https://doi.org/10.1016/S1359-4311(96)00071-3

31. Triplett KA, Ghiaasiaan SM, Abdel-Khalik SI, Sadowski DL (1999) Gas–liquid two-phase flow in microchannels Part I: two-phase flow patterns. Int J Multiph Flow 25(3):377–394. https://doi.org/10.1016/S0301-9322(98)00054-8

32. Ullmann A, Brauner N (2017) The prediction of flow pattern maps in minichannels. Multiph Sci Technol 19(1). https://doi.org/10.1615/MultScienTechn.v19.i1.20

33. Mudawar I (2001) Assessment of high-heat-flux thermal management schemes. IEEE Trans Compon Packag Technol 24(2):122–141. https://doi.org/10.1109/6144.926375

34. Schreiber M, Wits WW, te Riele GJ (2016) Numerical and experimental investigation of a counter-current two-phase thermosyphon with cascading pools. Appl Therm Eng 99:133–146. https://doi.org/10.1016/j.applthermaleng.2015.12.095

35. Zwier MP, van Gerner HJ, Wits WW (2017) Modelling and experimental investigation of a thermally driven self-oscillating pump. Appl Therm Eng 126:1126–1133. https://doi.org/10.1016/j.applthermaleng.2017.02.063

36. Huber M, Harvey A, Lemmon E, Hardin G, Bell I, McLinden M (2018) NIST Reference Fluid Thermodynamic and Transport Properties Database (REFPROP) Version 10 - SRD 23. National Institute of Standards and Technology. https://doi.org/10.18434/T4/1502528

37. Kim S-M, Mudawar I (2014) Review of databases and predictive methods for heat transfer in condensing and boiling mini/microchannel flows. Int J Heat Mass Transf 77:627–652. https://doi.org/10.1016/j.ijheatmasstransfer.2014.05.036

38. Müller-Steinhagen H, Heck K (1986) A simple friction pressure drop correlation for two-phase flow in pipes. Chem Eng Process Process Intensif 20(6):297–308. https://doi.org/10.1016/0255-2701(86)80008-3

39. Xu Y, Fang X, Su X, Zhou Z, Chen W (2013) Evaluation of frictional pressure drop correlations for two-phase flow in pipes. Nucl Eng Des 253:86–97. https://doi.org/10.1016/j.nucengdes.2012.08.007

40. Kim S-M, Mudawar I (2012) Universal approach to predicting two-phase frictional pressure drop for adiabatic and condensing mini/micro-channel flows. Int J Heat Mass Transf

55(11):3246–3261. https://doi.org/10.1016/j.ijheatmasstransfer.2012.02.047

41. Çengel YA, Cimbala JM (2014) Fluid mechanics: fundamentals and applications, 3rd edn. McGraw Hill, New York

42. Gladwell I, Shampine L, Thompson S (2003) Solving ODEs with MATLAB. Cambridge University Press

43. Kim S-M, Mudawar I (2013) Universal approach to predicting saturated flow boiling heat transfer in mini/micro-channels – Part II. Two-phase heat transfer coefficient. Int J Heat Mass Transf 64:1239–1256. https://doi.org/10.1016/j.ijheatmasstransfer.2013.04.014

44. Pettersen J, Rieberer R, Munkejord ST (2000) Heat transfer and pressure drop characteristics of evaporating carbon dioxide in microchannel tubes. 9